Journal of Sound and Vibration (1998) **209**(2), 343–372

SCATTERING BY CRACKS BENEATH FLUID–SOLID INTERFACES

R. V. Craster*

Department of Theoretical Mechanics, University of Nottingham, Nottingham, NG7 2RD, U.K.

(*Received* 10 *January* 1997, *and in final form* 4 *August* 1997)

The scattering of incident plane elastic, or fluid, body waves and interfacial waves by an arbitrarily orientated subsurface crack is considered. The crack lies in an infinite elastic half-space that is coupled to an overlying fluid half-space. Material parameters relevant for water–metal and water–rock combinations are taken and far field scattering patterns are given; these demonstrate beam formation along critical angles. For light, or moderate, fluid coupling, it is shown that the beams form along different critical angles depending upon the magnitude of the coupling.

In addition, reciprocity relations relating the far field scattering coefficients viewed along an angle θ, and generated by one type of plane wave incident along ϕ, to the scattering coefficient viewed along ϕ, generated by another plane wave incident along θ, are found. Reciprocity relations involving interfacial waves are also given.

Power flow theorems are derived; these relate the time averaged scattered power to a combination of far field scattering coefficients. This is used to determine the proportion of scattered power converted into the different types of scattered wave. The reciprocity and power flow theorems provide a powerful consistency check upon the numerical accuracy of the results.

The boundary value problem is recast as a system of coupled integro-differential equations for the unknown jump in displacement across the crack faces. These integral equations are solved in an efficient and fast numerical manner by performing the integrations over the crack faces analytically, thus reducing the computational effort substantially.

1. INTRODUCTION

A crack that lies beneath the surface of an elastic solid has a considerable influence upon the failure characteristics of the solid. Thus it is important to detect, and accurately determine the position of, cracks. The non-destructive testing of a solid to detect such flaws is often undertaken with the solid immersed in a fluid. The solid is then imaged by waves incident from the fluid. For line source excitation surface waves are generated that impinge upon defects near the surface, giving a strong signal. Alternatively, the material can be imaged using either incident surface waves or elastic body waves. The aim of this paper is to provide a mathematical analysis of the underlying physical problem and extract all the quantities of physical interest in an efficient and accurate manner. A subsurface crack is imaged by incident plane harmonic compressional waves from the fluid, or compressional and shear waves from the solid. In addition, incident interfacial waves are also considered. The far field responses are found.

*Currently visiting: Department of Mathematics, Imperial College, London, SW7 2AZ, U.K.

0022–460X/98/020343 + 30 $25.00/0/sv971252

In brief, the dominant far field responses that are generated are cylindrical shear or compressional body waves in the solid and a cylindrical compressional wave in the fluid. In addition, a Stoneley wave, often called the Schölte wave, is generated, and this is an unattenuated interfacial wave that decays exponentially with depth in both materials. In the absence of the overlying fluid the corresponding unattenuated surface wave is a Rayleigh wave. One interesting aspect is that the limiting process as the fluid coupling tends to zero is non-uniform; that is, the Rayleigh wave is not related to the Schölte wave even when the coupling tends to zero. In fact, in this limit the wave speed of the Schölte wave is typically slightly less than the compressional wave speed of the fluid. In the limit as the coupling tends to zero, one can unambiguously identify a leaky Rayleigh wave. This is a perturbation of the usual Rayleigh wave that now decays exponentially with distance along the interface from its source of excitation. The light fluid loading limit is important for applications; hence there will be an emphasis upon results associated with this limit.

There are also head waves generated in both the fluid and solid that decay faster than the cylindrical body waves; these head waves are generated as the cylindrical body waves do not satisfy the interfacial boundary conditions correctly. If the wave speed of the fluid is less than the shear wave speed of the solid, then the head waves generated by the acoustic cylindrical wave in the solid are evanescent. It will be implicitly assumed here that the shear wave speed of the solid is greater than the compressional wave speed of the fluid. This is usually the case: exceptions are combinations such as plastic/water interfaces. The analysis presented does not depend upon this assumption. A schematic, given in Figure 1, shows the wavefronts.

In the absence of the fluid, several scattering problems of this type have been treated by, for instance, Mendelsohn *et al*. [1] for surface breaking perpendicular cracks, Achenbach *et al*. [2] for subsurface parallel cracks, Brind and Achenbach [3] for subsurface

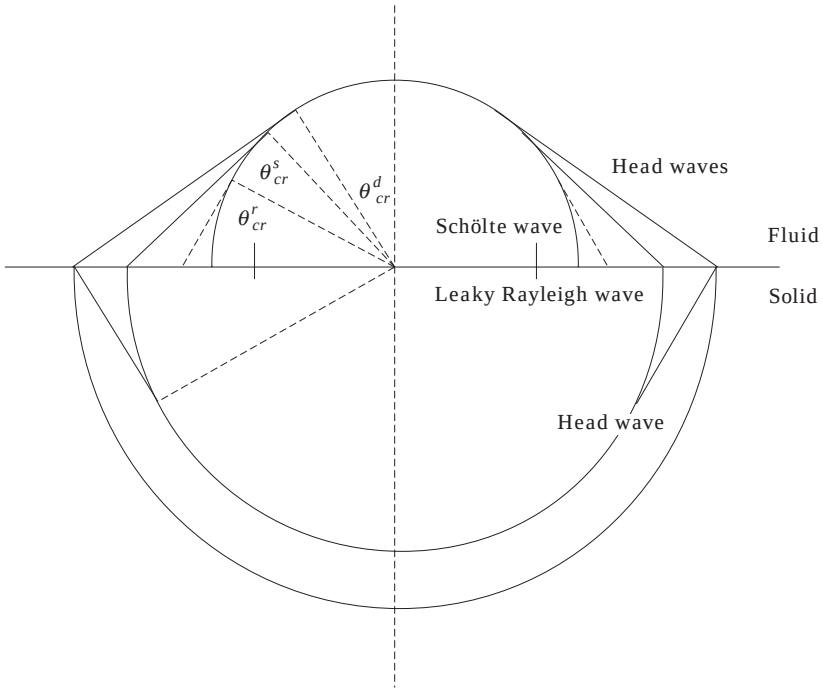

Figure 1. A schematic showing the scattered wavefronts in the far field for the situation in which the compressional wave speed in the fluid is less than the shear wave speed in the solid. In the right hand side of the schematic the leaky Rayleigh response is shown by the dashed line.

perpendicular cracks, and Van der Hijden and Neerhoff [4] for subsurface cracks of arbitrary orientation. For parallel cracks interesting near surface resonances in the stress intensity factors and transmission/reflection coefficients for Rayleigh waves (Keer *et al*. [5], Van der Hijden and Neerhoff [6]) were detected due to Lamb waves trapped between the crack and the interface.

With the addition of fluid loading there are fewer analyses: some exceptions are Gracewski and Bogy [7] and Ahn *et al*. [8]. The former treat a more general case in at least one sense, that of a subsurface parallel crack in a material with an elastic layer and substrate. The crack lies at the interface of the layer and substrate; and the material constants are chosen to prohibit any oscillatory singularities at the crack tips. The numerical procedure adopted is less efficient than that taken here and the results presented are limited; indeed, the authors stress that the amount of computer time required is not inconsequential. Reference [8] treats a surface breaking crack using boundary element methods incorporating the full space elastic Green function, and hence requiring elements both along the surface and along the crack faces. Boundary element methods do, however, have an additional flexibility in that finite domains can be treated; the analysis in this paper is restricted to unbounded domains.

In a series of papers, Neerhoff [9], Neerhoff and Van der Hijden [10], Van der Hijden and Neerhoff [4, 6, 11] considered several wave–crack interaction problems in either an elastic half-space or an infinite body. Their approach had several advantages over other contemporaneous works: rapid and accurate numerical evaluation, simple extensions allowing arbitrary crack orientation, elegant expressions for the stress intensity factors, far field directivities, and transmission/reflection coefficients for Rayleigh waves. Thus the method advocated in reference [4] is adopted in the present paper. By performing various integrations along the crack surfaces analytically, rather than numerically as in the standard approach to such problems, adopted in, for instance, reference [7], leads to fast and accurate numerical solutions. In turn, this enables a more detailed examination of the results than is convenient using the standard approach; in particular, the form of the eigensolutions adopted leads in a natural way to elegant expressions for far field scattering coefficients and stress intensity factors. For the fluid–solid problems the scattered far field within the fluid is of considerable interest; this paper is an extension of the approach adopted by Van der Hijden and Neerhoff [4] to the fluid–solid situation.

In addition, reciprocity and power flow theorems are derived: these provide useful consistency checks upon the numerical approach. Early authors such as Tan [12] concentrated upon theorems for obstacles within an infinite elastic domain, and Neerhoff [13] proved various theorems for obstacles within a half-space; these were extended to three dimensions by Rogoff [15]. Here the additional difficulties of adding an overlying fluid are incorporated, with the consequent changes that this introduces.

The plan of this paper is as follows: in section 2 the constitutive relations and crack geometries are described. Using suitable Green functions, coupled integral equations are formulated in section 3 for the scattering problems, and these are related to the fields within the solid and fluid. The integral equations are solved in a semi-analytical fashion; results are shown and discussed in section 4. In section 5, reciprocity and power flow theorems are presented. Much of the analytical detail is relegated to the appendices.

2. CONSTITUTIVE RELATIONS

An isotropic, homogeneous elastic solid lies in the half-space $x_3' > 0$ and a compressible fluid lies in $x_3' < 0$. The responses of the two materials are coupled together through continuity conditions along the interface $x_3' = 0$; these conditions are continuity of normal

stress and displacement. Time harmonic vibrations of frequency ω are considered, and all physical variables are assumed to have an $e^{-i\omega t}$ dependence: this is considered to be understood and is suppressed henceforth.

The elastic material has Lamé constants λ and μ, and density ρ. The stresses, σ_{ij}, are related to the displacements, u_i, via

$$\sigma_{ij} = \lambda\varepsilon_{kk}\delta_{ij} + 2\mu\varepsilon_{ij}, \qquad \text{with the strains } \varepsilon_{ij} = \tfrac{1}{2}(u_{i,j} + u_{j,i}). \tag{2.1}$$

The governing equations in the elastic solid are $\sigma_{ij,j} = -\rho\omega^2 u_i$. The elastic solid supports compressional and shear waves with wave speeds c_p and c_s respectively. They are defined as

$$c_p^2 = \frac{(\lambda + 2\mu)}{\rho}, \qquad c_s^2 = \frac{\mu}{\rho}.$$

The corresponding wavenumbers are k_p and k_s, defined as ω/c_p and ω/c_s; the following inequality is satisfied: $k_s > k_p$.

The compressible fluid in $x_3' < 0$ is effectively an elastic material supporting no shear stresses: thus $\sigma_{ij} = \lambda_f\varepsilon_{kk}\delta_{ij}$. The material has density ρ_f and compressional modulus λ_f, and supports a compressional wave with wave speed $c_0^2 = \lambda_f/\rho_f$.

In the absence of the fluid, a surface Rayleigh wave propagates with wave speed c_r and associated wavenumber k_r; $k_r > k_s$. It is also assumed here that $k_r < k_0$. This is usually the case and it ensures that the Rayleigh angle, to be defined later, is real; in this situation, distinctive beam formation is possible along the Rayleigh angle within the fluid. With the fluid present, the Schölte wave replaces the Rayleigh wave as the unattenuated interfacial wave; the wave speed is c_{sch} and $k_{sch} > k_0$. The Schölte wave speed is given explicitly as an integral in equation (D.15).

The assumption that the compressional wave speed of the fluid is less than the shear wave speed of the solid implies that $k_0 > k_s > k_p$.

During the analysis a coupling parameter ε naturally occurs; it is defined as $\varepsilon = \rho_f k_p/\rho k_0$, where k_p, k_0 are the wave speeds associated with compressional waves in the solid and fluid respectively. The coupling parameter is the ratio of fluid and solid impedances relative to the compressional waves and gives a measure of the coupling between fluid and solid disturbances, typically with water as the coupling fluid: $0{\cdot}05 \leqslant \varepsilon \leqslant 0{\cdot}3$. The limit when $\varepsilon \to 0$ is the light fluid loading limit; this is relevant for water–metal combinations. In this limit, one might expect that $k_{sch} \to k_r$; however, this is not the case and $k_{sch} \to k_0$, and the Rayleigh wave speed is perturbed to include a small imaginary part that leads to the energy leakage into the fluid and exponential decay with distance along the interface.

3. FORMULATION OF THE INTEGRAL EQUATIONS

The subsurface crack geometry and boundary conditions are shown in Figure 2; the types of incident wave are shown in Figure 3. Two related Cartesian co-ordinate systems are shown in Figure 2; one is the x_1', x_3' system based upon the interface, and the other is the x_1, x_3 system based upon the crack. The origin of the crack system is displaced a distance d from that of the interfacial system and lies at the center of the crack. The crack is of length $2a$ and $|x_1| < a$. The co-ordinate systems are related via a displacement and rotation as $x_1' = x_1\cos\theta + x_3\sin\theta$, $x_3' = -x_1\sin\theta + x_3\cos\theta + d$. The two co-ordinate systems are used within the text. The notation u_3, $u_{3'}$ is used to denote variables relative to the different co-ordinate systems.

The crack is taken to be stress free, so that $\sigma_{13} = \sigma_{33} = 0$ on $x_3 = 0$, $|x_1| < a$. Thus the crack faces are assumed not to interact with each other: this is a viable assumption if we

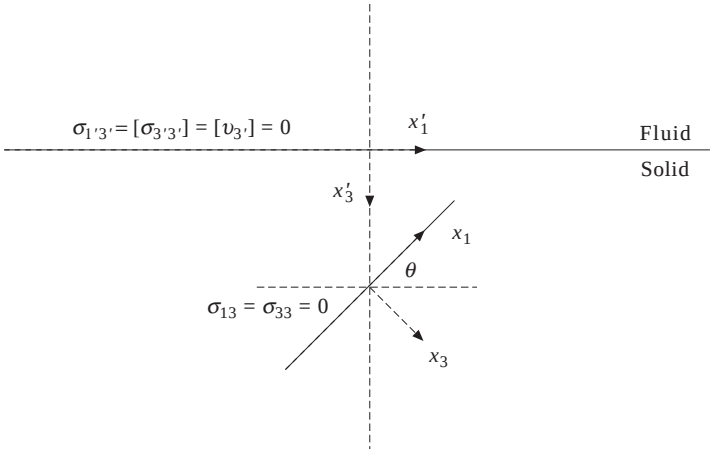

Figure 2. The co-ordinate system associated with the subsurface crack and the boundary conditions. The crack is stress free and is shown by the solid line in the x_1 direction.

are modelling an open crack of finite width. The stresses have the usual inverse square root dependence upon the radial distance from the crack tips; see, e.g., Williams [16]. The scattered field satisfies the radiation condition; that is, we have outgoing waves at infinity. Along the interface the shear stress is zero and the fluid supports no shear; thus $\sigma_{1'3'} = 0$ on $x_3' = 0$. Continuity of normal stress and displacement on the interface leads to $[\sigma_{3'3'}] = [u_{3'}] = 0$ on $x_3' = 0$. The notation $[u]$ denotes the jump $u(x_1, x_3 = 0_+) - u(x_1, x_3 = 0_-)$.

The displacement jump across the crack faces is not known and is denoted by

$$\mathbf{\Psi}_\alpha(x_1) = [u_\alpha(x_1, 0)], \qquad |x_1| < a, \quad \alpha = 1, 3. \tag{3.1}$$

The aim of the following is to determine an integral equation for this displacement jump; once this jump is found, the scattered fields are related to integrals involving this quantity.

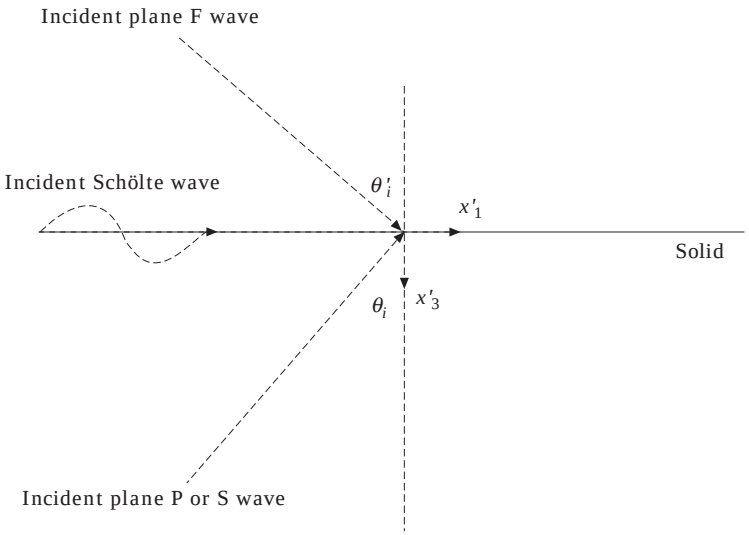

Figure 3. The incident wave fields.

The total field is split into incident and scattered pieces, so that $u^{total} = u^{in} + u^{sc}$, with similar representations for the stresses. The integral equations are formulated in terms of the scattered field. The incident fields are taken to be either plane elastic body waves, P or S waves, or a compressional plane wave in the fluid: here it is called an F wave, or an incident Schölte wave.

Utilizing the reciprocal theorem

$$\int_V (\sigma_{ij,j}u_i^* - \sigma_{ij,j}^* u_i)\,\mathrm{d}V = \int_S (\sigma_{ij}u_i^* - \sigma_{ij}^* u_i)n_j\,\mathrm{d}S \tag{3.2}$$

that relates two independent states, the starred and unstarred fields, within a volume V with surface S (n_j is the outward pointing normal) the following integral representation for the scattered field at a point (p_1, p_3) within either the solid or fluid is found:

$$u_k^{sc}(p_1, p_3) = \int_{-a}^{a} \sigma_{i3;k}^G(x_1, 0; p_1, p_3)[u_i^{sc}(x_1, 0)]\,\mathrm{d}x_1. \tag{3.3}$$

The summation convention is adopted over repeated suffices. The notation $\sigma_{ij,j}$ is used to represent differentiation of σ_{ij} with respect to x_j, whereas the stress tensor $\sigma_{ij;k}^G$ is the Green function associated with point forces in the x_1, x_3 directions; i.e., perpendicular or parallel to the crack faces. It is the Green's state following from the solution of

$$\sigma_{kj,j}^G(\mathbf{x}; \mathbf{p}) + \rho\omega^2 u_k^G(\mathbf{x}; \mathbf{p}) = -f_k\delta(\mathbf{x} - \mathbf{p}), \tag{3.4}$$

where f_k is the unit vector. The reciprocal theorem is used with the scattered field as one state and using a solution associated with the Green's state as the other; the Green function is given explicitly in Appendix C. In equation (3.4) above, the delta function is the two-dimensional delta function and the term $[u_i^{sc}(x_1, 0)]$ that occurs in equation (3.3) is the unknown jump in the displacement induced by the incident field across the crack faces. Integro-differential equations for these terms, written from now onwards as $\mathbf{\Psi}_i(x_1)$, are found by substituting equation (3.3) into the constitutive relation (2.1) and then taking the limit as $p_3 \to 0$. In conjunction with the stress free crack faces condition, the integro-differential equations are

$$-\sigma_{i3}^{in}(p_1, 0) = \lambda\delta_{i3}\frac{\partial}{\partial p_k}\int_{-a}^{a}\sigma_{j3;k}^G\mathbf{\Psi}_j\,\mathrm{d}x_1 + \mu\frac{\partial}{\partial p_3}\int_{-a}^{a}\sigma_{j3;i}^G\mathbf{\Psi}_j\,\mathrm{d}x_1 + \mu\frac{\partial}{\partial p_i}\int_{-a}^{a}\sigma_{j3;3}^G\mathbf{\Psi}_j\,\mathrm{d}x_1 \tag{3.5}$$

for $i = 1, 3$ and as $p_3 \to 0$ for $|x_1| < a$. The argument for the stresses is $(x_1, 0; p_1, p_3)$ and that of $\mathbf{\Psi}$ is (x_1). These integro-differential equations are treated by expanding the unknowns as a sequence of Chebyshev polynomials; that is,

$$\mathbf{\Psi}_\alpha(x_1) = \frac{4}{i}\sum_{n=1}^{\infty} a_{\alpha;n}\psi_n(x_1), \qquad \text{where } \psi_n(x_1) = \begin{cases}\cos(n \arcsin(x_1/a)) & n \text{ odd},\\ \mathrm{i}\sin(n \arcsin(x_1/a)) & n \text{ even},\end{cases} \tag{3.6}$$

for $\alpha = 1, 3$ where the $a_{\alpha;n}$ are to be determined. These are the natural eigenfunctions and incorporate the correct edge behaviour.

Both sides of equation (3.5) are multiplied by the complex conjugate of a term of equation (3.6) and integrated over the crack faces; complex conjugates are denoted by an

overbar. Recalling that the Green function is represented in Appendix C as a Fourier transform, all of the integrations over the crack faces are done analytically using

$$\int_{-a}^{a} \bar{\psi}_m(x_1)\, \mathrm{e}^{\mathrm{i}kx_1}\, \mathrm{d}x_1 = \frac{\pi m}{k}\, \mathrm{J}_m(ka) \tag{3.7}$$

and related integrals; the $\mathrm{J}_m(ka)$ are Bessel functions of the first kind. This sequence of operations yields the set of simultaneous equations

$$b_{i;m} = \sum_{n=1}^{\infty} K_{ij;mn} a_{j;n}, \qquad m = 1, 2, 3, \ldots \tag{3.8}$$

and $i = 1, 3$. The kernel functions $K_{ij;mn}$ are given as integrals involving Bessel functions in Appendix B. The left side is known in terms of the incident field

$$b_{i;m} = -\frac{1}{\mu\pi} \int_{-a}^{a} \sigma_{i3}^{in}(x_1, 0) \bar{\psi}_m(x_1)\, \mathrm{d}x_1 \qquad \text{for } i = 1, 3. \tag{3.9}$$

For the incident plane and surface waves this integral is evaluated explicitly and is given in Appendix D. For more general incident fields due, say, to a line source in the fluid, this integral must be done numerically. The integrals in the kernel functions are manipulated so that they can be performed using standard numerical integration routines; this is discussed in Appendix B. The sum in equation (3.8) is truncated at some value of N, chosen so that the relative difference between the variables of interest is less than a specified error. The matrix inversion to identify the $a_{j;n}$ is performed using standard Linpack routines. Once these $a_{j;n}$ are known, then $\mathbf{\Psi}_i$ is identified and the scattered field in equation (3.3) is now known. These representations contain the Green function explicitly as an inverse Fourier transform; hence the far field form of the scattered fields is easily deduced. In addition, this is convenient, as one can take advantage of previous transform analyses of similar Green's functions [17] to extract the non-uniform behaviour that occurs in the neighbourhood of the Rayleigh angle for $1 \ll k_0 r \ll 1/\varepsilon^2$, although we shall not present those results here.

4. RESULTS

In this section the scattered fields and stress intensity factors are discussed for waves incident upon cracks either parallel to, or perpendicular to, the interface. Numerical results are available for other angles and these are to be presented elsewhere. The far field scattering coefficients are normalized, and the functions

$$\bar{G}_P(\phi) = \frac{\omega(\lambda + 2\mu)}{16\pi[P_{body}]} |G_P(\theta_i, \phi)|^2, \qquad \bar{G}_S(\phi) = \frac{\omega\mu}{16\pi[P_{body}]} |G_S(\theta_i, \phi)|^2, \tag{4.1}$$

$$\bar{G}_F(\phi') = \frac{\omega\lambda_f}{16\pi[P_{body}]} |G_F(\theta_i, \phi')|^2 \tag{4.2}$$

are used in the figures showing far field scattered wave patterns. The proportion of the total time average power converted to body waves is $[P_{body}]$—see equation (5.13)—and the functions $G_{P,S,F}$ are the directivities for the scattered cylindrical waves defined in section 5.1 and given explicitly in Appendix D. Hence $\bar{G}_{P,S,F}(\phi)$ are the directivity gains along a ray. The power converted to body waves depends upon the incident wave and material

parameters: to enable comparison between figures involving the $\bar{G}$, the value of $16P_{body}/\omega(\lambda + 2\mu) = P_B$ is given for each figure.

The parameters $k_s a$, d and ε will be varied. The first set of material parameters taken are $k_p = \frac{1}{2}k_s$, $k_0 = 3k_s$. These are typical of metal–water combinations; that is, of solids with relatively high densities and wave speeds relative to the fluid. For instance, for aluminium–water, aluminium has a density of 2698 kg/m^3 and longitudinal and shear wave speeds of 6374 m/s and 3111 m/s respectively (and would, if the water was replaced by a vacuum, have a Rayleigh wave speed of 2905·9 m/s. Water has a density of 1000 kg/m^3 and a longitudinal wave speed of 1480 m/s; the Schölte wave speed is 1476·7 m/s. Note that the Schölte wave speed is very close to the compressional wave speed of the fluid. For the aluminium–water combination, $\varepsilon = 0{\cdot}08606$. For $k_p = \frac{1}{2}k_s$ and $k_0 = 3k_s$ the Rayleigh wave speed (in the absence of the fluid) is $k_r = 1{\cdot}0723k_s$: if $\varepsilon = 0{\cdot}08$, then $k_{sch} = 1{\cdot}00075k_0$.

The second set of material parameters used are as follows: $k_d = 2k_s/3$, $k_0 = 4k_s/3$, $\varepsilon = 0{\cdot}3$. This implies that $\rho = 5\rho_f/3$, $k_r = 1{\cdot}12k_s$ and $k_{sch} = 1{\cdot}068k_0$. These are more typical of rock–water combinations; for instance, for sandstone–water, $c_d = 2920$ m/s and $c_s = 1840$ m/s, the material parameters being taken from Briggs [18], and $c_r = 1677$ m/s with $c_{sch} = 1385$ m/s.

These two different sets of material parameters will demonstrate the effect of light fluid coupling (the water–metal case) and moderate fluid loading (the rock–water case). The magnitude of the coupling is crucial to the form of the scattered field.

In the following discussions, critical angles will be discussed; see Figure 1. In the solid a head wave is generated and the wavefronts propagate into the solid where the wavefront normals subtend angles $\pm\sin^{-1}(c_s/c_d)$ to the x_3-axis. In the fluid, two head waves are generated by the shear and compressional waves in the solid: these propagate into the fluid and the wavefront normals subtend angles $\pm\theta^d_{cr}$, where $\theta^d_{cr} = \sin^{-1}(c_0/c_d)$, and $\pm\theta^s_{cr}$, where $\theta^s_{cr} = \sin^{-1}(c_0/c_s)$ to the $-x_3$-axis. In addition, for small ε, the Rayleigh wave is perturbed into a leaky Rayleigh wave. This leaky Rayleigh wave sheds energy into the fluid along angles $\pm\theta^r_{cr}$, where $\theta^r_{cr} = \sin^{-1}(c_0/c_r)$ (see, for instance, Brekhovskikh [19]); these are known as the Rayleigh angles. A detailed discussion of these wavefronts for transient disturbances is contained in Craster [20]. The critical angles are important, as the dominant features of the directivity patterns involve beam formation along these angles.

The stress intensity factors characterize the near crack tip stress fields [16]. Following Van der Hijden and Neerhoff [4], the displacement jumps near the crack tips are

$$\mathbf{\Psi}_l(x_1) \sim \frac{2(1-\nu)}{\mu}\sqrt{2}K_j^{\pm}(a \mp x)^{1/2} \qquad \text{as } x_1 \to \pm a \tag{4.3}$$

if $l = 1, j = 2$, and if $l = 3, j = 1$, with ν being the Poisson ratio; and with an appropriate normalization of the stress intensity factors (see reference [21]), $K_j^{\pm}$ is

$$|k_j^{\pm}| = \frac{|K_j^{\pm}|}{(\lambda + 2\mu)k_p a^{1/2}} \tag{4.4}$$

for an incident P wave. The same notation is used for incident F or Schölte waves. In the case of S waves, μ replaces $(\lambda + 2\mu)$ and S replaces P. The mode 1, $K_1^{\pm}$, stress intensity factors characterize the opening tensile stresses at the crack tips and the mode 2, $K_2^{\pm}$, stress intensity factors characterize the shear stresses at the crack tips.

In terms of the coefficients $a_{z;n}$, these are concisely given by

$$|k_j^{\pm}| = \frac{2\mu}{k_p a(\lambda + 2\mu)(1-\nu)}\left|\sum_{n=1}^{\infty} i(\pm i)^{n+1} n a_{l;n}\right|. \tag{4.5}$$

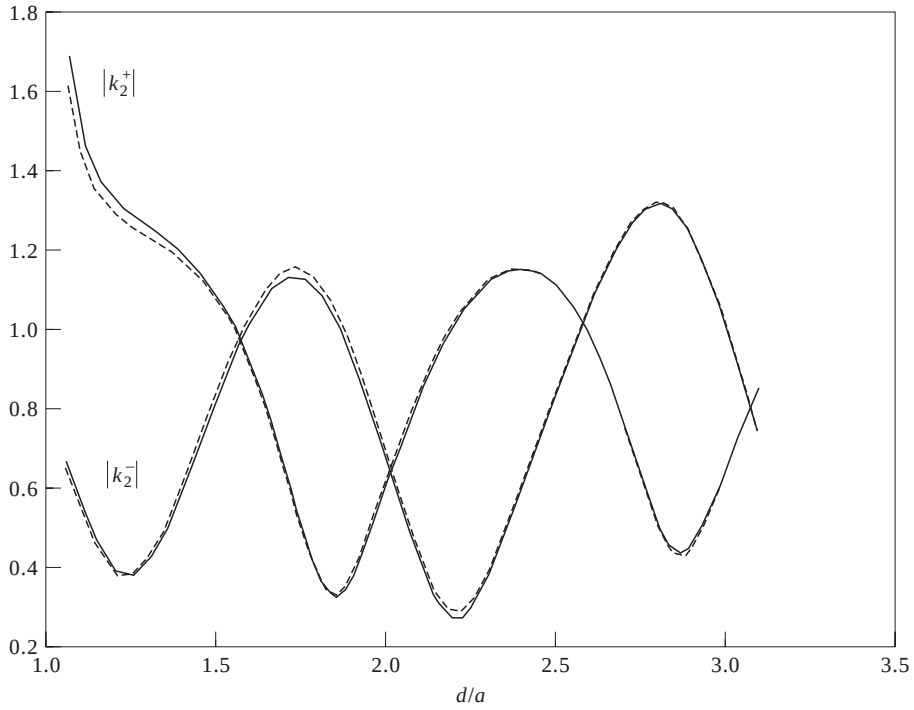

Figure 4. The stress intensity factors for a crack perpendicular to the interface with an incident plane S wave, $k_s a = 3$ and $\theta_i = 0$. The coupling parameters are $\varepsilon = 0$ (——) and $\varepsilon = 0{\cdot}3$ (----).

In the case of incident elastic body waves, for small ε, the presence of the fluid has a minimal effect upon the stress intensity factors. This concurs with the general idea underlying an asymptotic light fluid loading approach (see Craster [22]); that is, the elastic and fluid problems can in many situations be separated, solved independently and then matched together. In Figure 4 are shown the stress intensity factors when a crack perpendicular to the interface is subject to an incident S wave along $\theta_i = 0$, $k_s a = 3$ and with varying d/a for $\varepsilon = 0$ and $0{\cdot}3$. Only the shear stress intensity factors appear in this figure, as there is no opening tensile loading upon the crack. For $\varepsilon = 0$, this figure appears in reference [4].

In Figure 5 are shown the stress intensity factors generated by an incident compressional wave from the fluid for a perpendicular crack with $k_s a = 3$, $\varepsilon = 0{\cdot}08$, $d/a = 1{\cdot}5$ and a varying angle of incidence θ_i'. The large peaks occur when θ_i' is one of the critical angles. For this example, $\theta_{cr}^r = 0{\cdot}37$, $\theta_{cr}^s = 0{\cdot}34$ and $\theta_{cr}^d = 0{\cdot}17$; this suggests that the largest interaction between the incident wave and crack occurs when the wave is incident along these angles. As d/a decreases, these stress intensity factors increase: the intensity factors at $x_1 = a$ ultimately tend to infinity as $d/a \to 1$.

The situation in which the crack is parallel to the surface and d/a is small is interesting, as resonances are detected and, as shown, in the absence of any fluid [5, 6] these are related to Lamb waves trapped between the crack and free surface. A related phenomenon occurs with the addition of the fluid and will be treated in detail elsewhere.

4.1. THE LIGHT FLUID LOADING CASE (METAL–WATER)

In this section, the parameters appropriate for a typical metal–water interface as described earlier are taken. Incident P and S waves generate the scattering patterns shown

in Figures 6–13. Initially, cracks parallel to the interface are considered: unless otherwise stated, the parameters taken are $k_s a = 3$, $d/a = 0{\cdot}5$ and $\varepsilon = 0{\cdot}08$. In the figures for scattering patterns, the functions $\bar{G}_{P,S,F}$ are plotted, where ϕ and ϕ' are taken in the same sense as θ_i, θ_i' in Figure 3. In Figures 6–13, the axes are x_1', $-x_3'$; the choice of co-ordinate systems earlier has the fluid in $x_3' < 0$ and the solid in $x_3' > 0$, so in these figures the fluid is above the solid. The solid line in the fluid is the directivity gain for the F wave and the solid/dashed lines in the solid are the directivity gains for the S and P waves respectively.

In Figure 6 an incident plane P wave along $\theta_i = \pi/4$ creates the scattering pattern, and distinctive beaming occurs in the fluid along one of the Rayleigh angles $\theta' = \theta_{cr}^r$ (one peak is off the figure and is at $(-4{\cdot}2, -11{\cdot}0)$), together with other peaks that are of a smaller magnitude. The sharpest of these smaller peaks in $\bar{G}_F$ occurs along $\theta' = -\theta_{cr}^d$; this is generated by the head wave associated with the compressional wave in the solid. Similarly, the sharp peak in $\bar{G}_S$ is generated by the head wave in the solid. The directivity gain $\bar{G}_P$ shows no particularly strong features; this is typically the case in most of the figures. It is interesting to note that the beam formation along the other Rayleigh angle, $\theta' = -\theta_{cr}^r$, is quite weak and smaller than that due to the head wave; this is perhaps unexpected. As the fluid loading is light this is rationalized by considering the same problem in the absence of the fluid and examining the scattered power converted into Rayleigh waves. With no fluid present, and taking the same incident wave, it turns out that a larger fraction of the total scattered power goes into the Rayleigh wave propagating towards $x_1' = -\infty$ (6%) rather than in the direction $x_1' = +\infty$ (0·3%). When the fluid is introduced, the beaming is in part generated by the leakage of energy from the Rayleigh waves into the fluid; thus this generates the larger beam along $\theta = \theta_{cr}^r$. The directivity gains in the solid found in the absence of the fluid are, as one would naturally expect in the light fluid loading limit, very

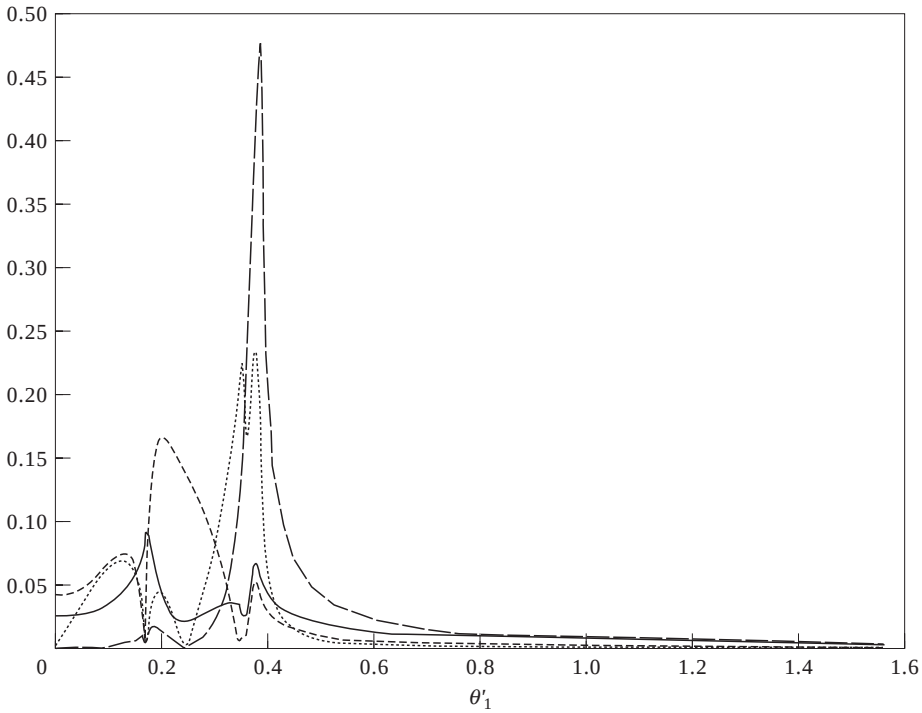

Figure 5. The stress intensity factors for a crack perpendicular to the interface subjected to an incident F wave with $k_s a = 3$, $d/a = 1{\cdot}5$, $\varepsilon = 0{\cdot}08$ and a varying angle of incidence. ——, $|k_1^+|$; ——, $|k_2^+|$; ----, $|k_1^-|$; · · · · , $|k_2^-|$.

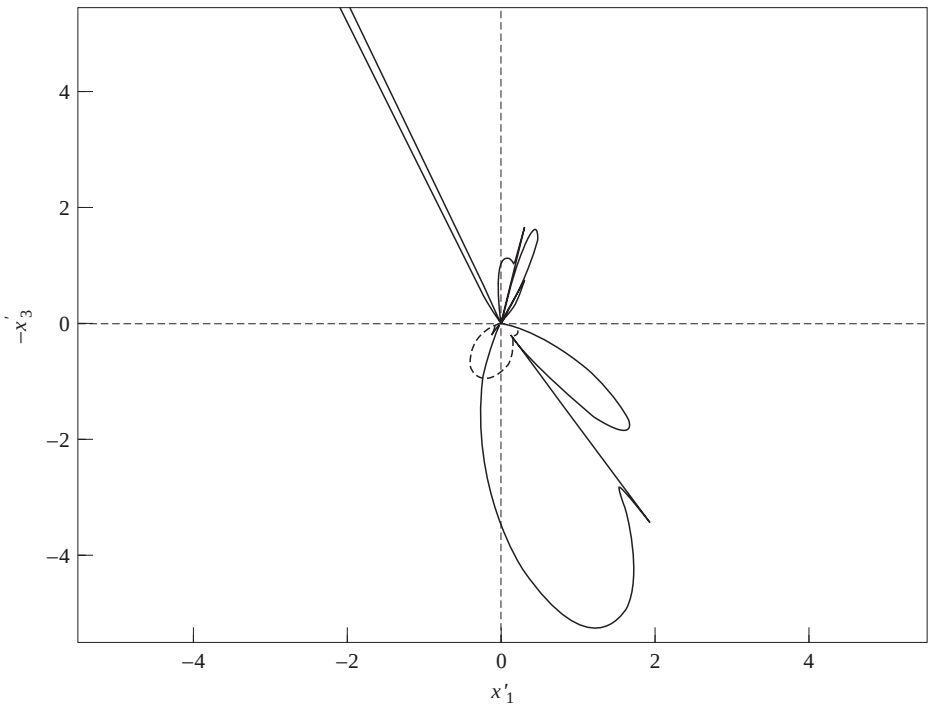

Figure 6. The directivity gains for an incident P wave along $\theta_i = \pi/4$, $k_s a = 3$, $\varepsilon = 0{\cdot}08$ and $d/a = 0{\cdot}5$ ($P_B = 44$). ——, S; ----, P; ——, F.

close to those found when $\varepsilon = 0{\cdot}08$. For the incident P wave along $\theta_i = \pi/4$, these are shown in Figure 7.

Increasing d/a leads to a larger response in the solid: for $d/a = 1$, $k_s a = 3$, $\varepsilon = 0{\cdot}08$ and $\theta_i = \pi/4$, the directivity gains are shown in Figure 8. Note that the beam formation is now dominant along $\theta_i = \theta_{cr}^r$; using the rationale above, in the absence of the fluid 2·5% of the scattered power is converted to Rayleigh waves propagating in the $+x_1$ direction versus 1% propagating in the $-x_1$ direction. Returning to the $d/a = 0{\cdot}5$ case, as one alters the angle of incidence towards $\theta_i = 0$, the beam along $\theta' = -\theta_{cr}^r$ becomes stronger, until it is of the same magnitude as that along the other Rayleigh angle. The scattering patterns for $\theta_i = 0$ are shown in Figure 9.

It might be envisaged that incident S waves would generate a weaker scattered field in the fluid due to the zero shear stress boundary condition at the interface. However, as we can see from Figure 10, this is not necessarily the case. Note that the main beam formation is now along $\theta' = -\theta_{cr}^r$; that is, it does not behave in a similar manner to the incident P wave with the same θ_i. The rationale is the same as that above: considering the same problem in the absence of the fluid, a substantial proportion of the power is converted into a Rayleigh wave propagating in the $+x_1'$ (23%) direction (the peak is off the figure and is at (13·9, −36·2)) and this creates the dominant beam; a not inconsequential fraction, 4%, is converted into Rayleigh waves in the direction $-x_1'$ and this gives the lesser beam along $\theta' = \theta_{cr}^r$.

Now consider incident plane waves from the fluid. If $k_0 \sin \theta_i' > k_s$ then the transmitted waves in the solid are inhomogeneous plane waves, the amplitude of which decays exponentially with depth. Hence a strong scattering pattern is only expected for cracks close to the interface ($d/a \leqslant 1$): as the waves are confined to the neighbourhood of the

interface there are strong interactions for cracks near to the interface. The maximal response is for $\theta_i' = \theta_{cr}'$; that is, along the Rayleigh angle. A wave from the fluid along $\theta' = \pi/4$ is shown in Figure 11: the beam formation along the Rayleigh angles is strongly dominant with little response in the solid, and a considerable fraction, 69%, of the scattered power is converted into the scattered wave in the fluid; thus this is a highly efficient method of imaging subsurface cracks. For $k_0 \sin \theta_i' \leqslant k_s$ the beam formation along the Rayleigh angles is still dominant, but less pronounced than, say that of Figure 11; the weakest response is for $\theta_i' = 0$.

In the situations considered above, almost no scattered power is converted into Schölte waves; this is in contrast to the power conversion to Rayleigh waves, when the fluid is absent, when there can be relatively large power conversion to Rayleigh waves, particularly for small $k_s a$. Schölte waves are thus hard to excite unless the crack is very close to the interface: in this case, resonance behaviour due to trapped Lamb modes, similar to references [5, 6], also may occur, and this issue will be dealt with elsewhere.

To demonstrate the effect of changing the crack orientation, a crack is now considered to be perpendicular to the interface. The relevant parameters in Figures 12 and 13 are $k_s a = 3$, $d/a = 1{\cdot}5$ and $\varepsilon = 0{\cdot}08$. The results for incident P and S waves are slightly different from the parallel crack case. Once more, we consider incident plane waves along $\theta_i = \pi/4$: for an incident plane P wave, the directivity gains are shown in Figure 12. Note that the beam formation in the fluid along the head wave angle associated with the solid compressional wave is almost of the same magnitude as that associated with Rayleigh wave. In the solid the beaming occurs along the critical angle associated with the head wave.

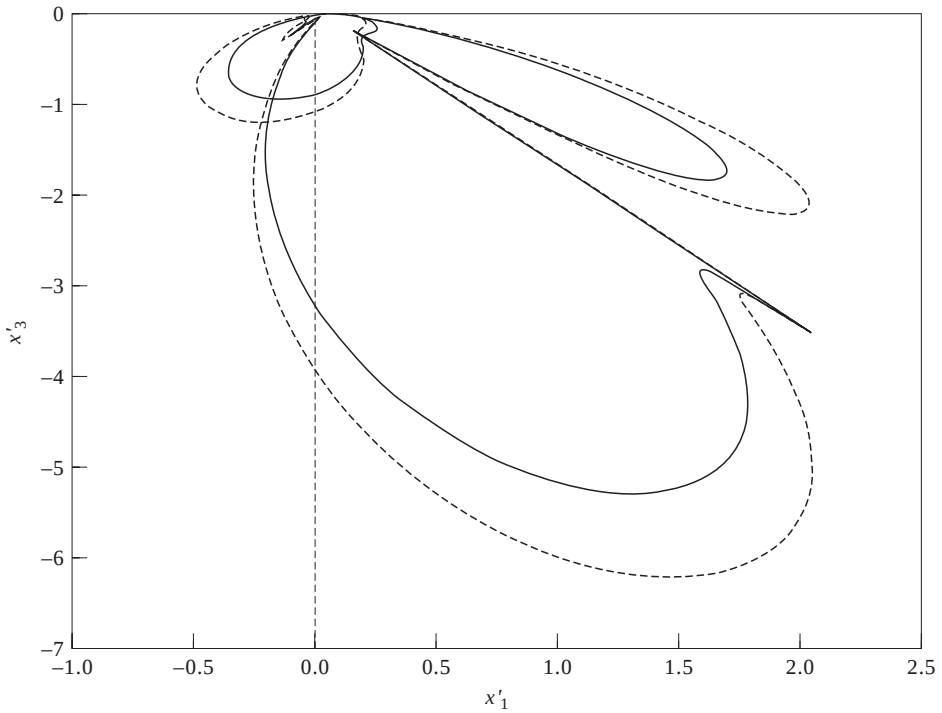

Figure 7. The directivity gains in the solid for an incident P wave along $\theta_i = \pi/4$, $k_s a = 3$ and $d/a = 0{\cdot}5$. ----, $\varepsilon = 0{\cdot}0$ ($P_B = 40$); ——, $\varepsilon = 0{\cdot}08$. The directivity gains $\bar{G}_s$ are the larger curves and $\bar{G}_p$ the smaller curves.

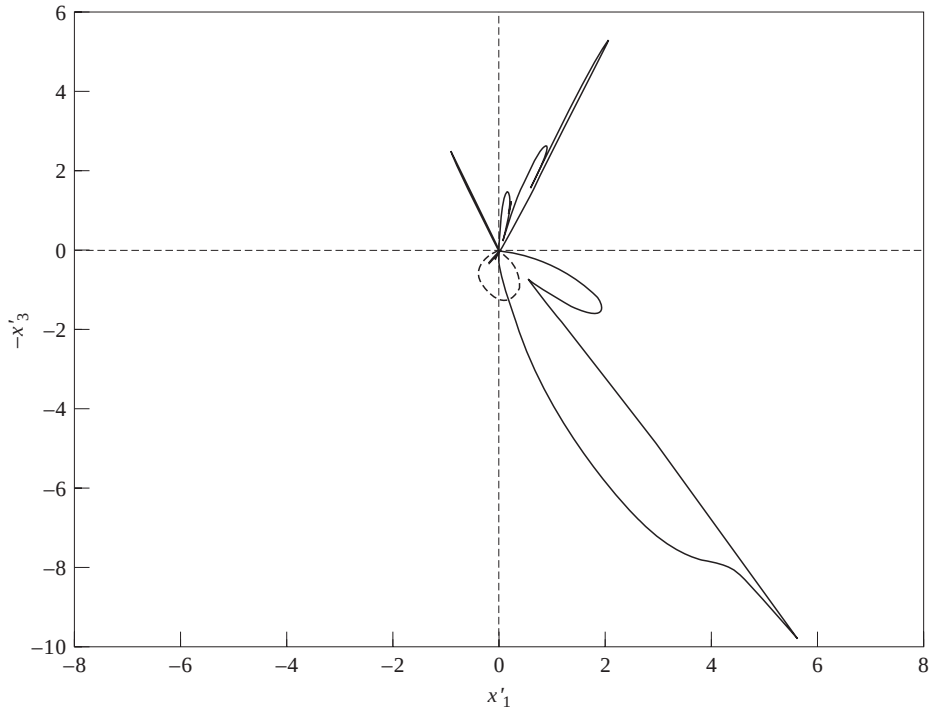

Figure 8. The directivity gains for an incident P wave along $\theta_i = \pi/4$, $k_s a = 3$, $\varepsilon = 0{\cdot}08$ and $d/a = 1{\cdot}0$ ($P_B = 62$). ——, S; ----, P; ——, F.

The scattered fields for an incident S wave along $\theta_i = \pi/4$ are symmetric for the specific choice of material parameters taken here; this angle of incidence is special, as the shear loading on the crack is then zero, and the crack is only subjected to a tensile opening stress and this leads to the symmetric scattered field. If one alters the angle of incidence to say, $\theta_i = \pi/3$, strong beam formation along the Rayleigh angles is once more evident.

It is interesting to note that a purely symmetric scattered field can also be generated, for the same reason, if the crack is imaged by an incident F wave along $\theta_i' = \pm \sin^{-1}(k_s/\sqrt{2k_0})$. For an incident plane F wave along $\theta_i' = \pi/4$, the scattered fields are shown in Figure 13; these gains are very similar to the parallel crack case shown in Figure 11, although the value for the total scattered power is quite different.

The far field scattering patterns shown above demonstrate considerable acoustic beaming within the fluid. It is also of interest to assess the proportion of scattered power that is converted into scattered power in the fluid. In Figure 14, the fraction of scattered power converted into P, S, F and Schölte waves for an incident plane P wave at $\theta_i = \pi/4$, for $k_s a = 3$, $\varepsilon = 0{\cdot}08$ and varying d/a, upon a perpendicular crack is shown; a considerable fraction of the scattered power is converted to power within the fluid and the fraction converted to Schölte waves is so small that it does not show in the figure. Thus a crack is a reasonably efficient scatterer of power into the fluid provided that the crack is close to the surface and it is hard to excite Schölte waves. In Figure 15 is shown the power conversion for the same case, except that now $\varepsilon = 0$. It is clear that the effect of fluid coupling is to convert the power that was carried by Rayleigh waves, and a proportion of that carried by elastic waves, into power in the fluid. Note that the total scattered power decreases as d/a increases, and that Figures 14 and 15 are showing the fraction of this converted to the different types of waves.

4.2. MODERATE FLUID LOADING (ROCK–WATER)

Far field directivities are now shown for the second set of material parameters, that are more relevant for rock–water systems. The coupling parameter ε is now increased to 0·3 and the solid has a lower compressional wave speed, with the shear wave speed greater than the compressional wave speed of the fluid; that is, $k_d = 2k_s/3$, $k_0 = 4k_s/3$. In Figures 16 and 17 are shown the directivities for incident P and F waves upon a crack parallel to the interface. In Figures 16 and 17, the two sharp peaks in the fluid directivity are formed along the critical angles associated with the head waves. Characteristic beams are now formed along these angles for the incident P and F waves instead of along the Rayleigh angles. These beams are not as dominant as those found in the previous section. The coupling parameter takes the value $\varepsilon = 0{\cdot}3$ in these figures, and $k_s a = 3$ and $d/a = 0{\cdot}5$ once again. Increasing the coupling leads to an increased response in the solid for incident F waves and a fundamental change in the nature of the scattering patterns. It is worth noting that beaming along the Rayleigh angles is not present for these material parameters for all the incident waves at the same ε as in the previous section; that is, for $\varepsilon = 0{\cdot}08$. For instance, for the material parameters taken here, beaming along the Rayleigh angles due to an incident plane P wave begins to occur for $\varepsilon \sim 0{\cdot}04$. The criterion for beaming to occur is that

$$\left| \frac{\varepsilon k_s^4 k_0 (k_r^2 - k_p^2)^{1/2}}{k_d k_r R'(k_r)(k_0^2 - k_r^2)^{1/2}} \right| \ll 1, \tag{4.6}$$

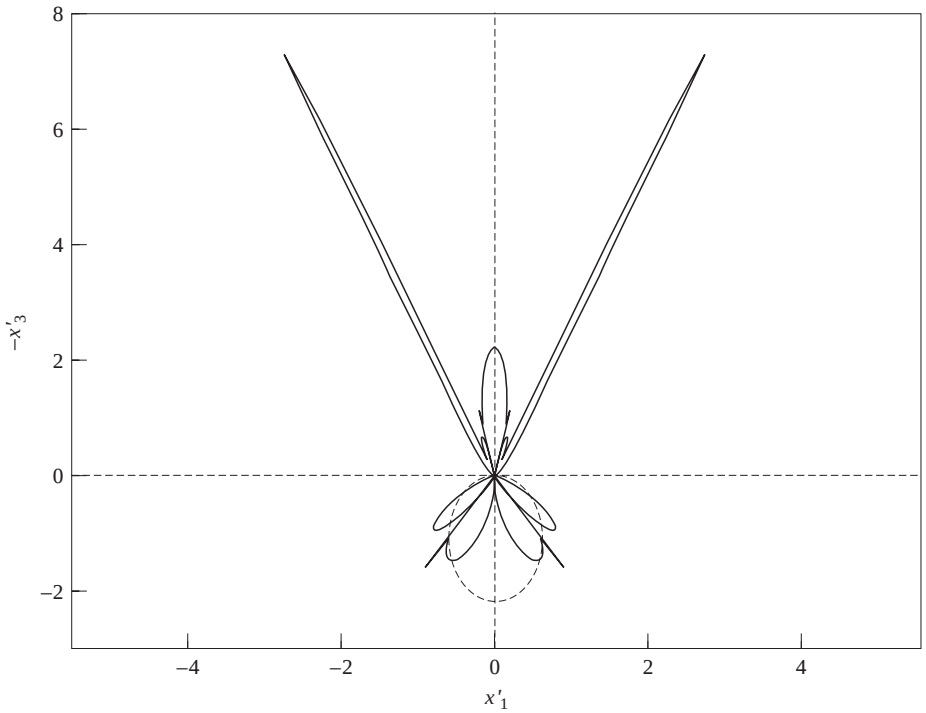

Figure 9. The directivity gains for an incident P wave along $\theta_i = 0$, $k_s a = 3$, $\varepsilon = 0{\cdot}08$ and $d/a = 0{\cdot}5$ ($P_B = 54$). ——, S; ----, P; ——, F.

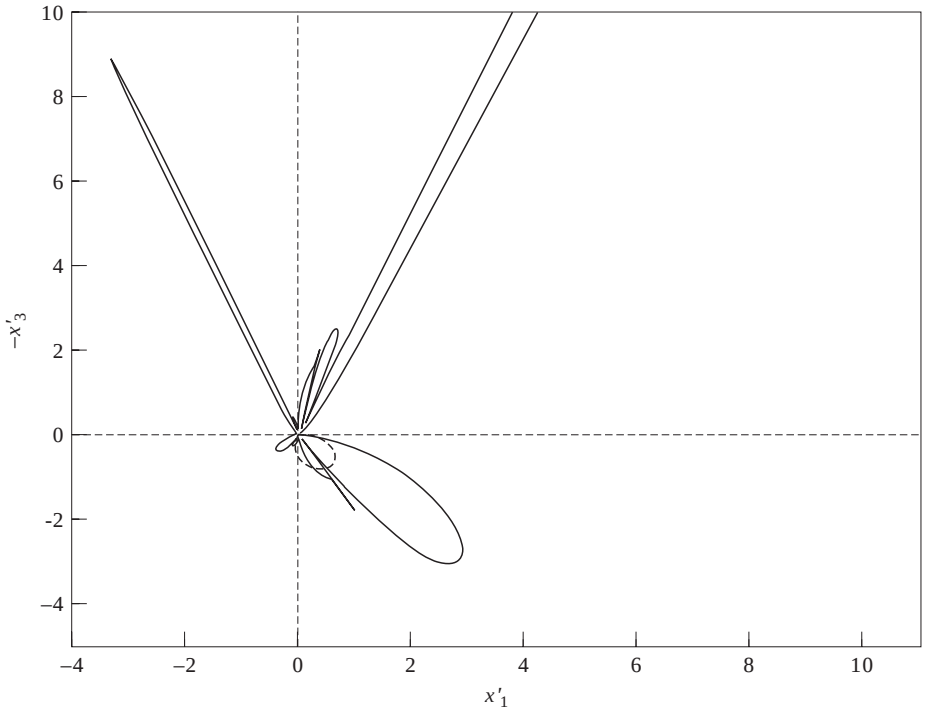

Figure 10. The directivity gains for an incident S wave along $\theta_i = \pi/4$, $k_s a = 3$, $\varepsilon = 0{\cdot}08$ and $d/a = 0{\cdot}5$ ($P_B = 29$). ——, S; ----, P; ——, F.

which depends upon the material constants. A similar change in the beaming occurs when the orientation of the crack is altered: scattering patterns for incident F and P waves upon a perpendicular crack are shown in Figures 18 and 19. The peaks in the fluid in Figure 19 are along the critical angle associated with the shear wave speed.

5. RECIPROCITY AND POWER FLOW THEOREMS

The wave–crack interaction problem considered in the main body of this paper contains several complicated manipulations and the numerical evaluation of the kernel functions is a slightly delicate operation: thus it is vital to have independent checks upon the numerical analysis. These do not appear to have been utilized by others considering fluid–solid interactions. Reciprocity and power flow theorems provide valuable consistency checks upon the numerical work; they are not independent checks upon the accuracy to which the physical problem is actually solved—see the comments at the end of this section. These theorems are also of interest in their own right.

5.1. RECIPROCITY THEOREMS

Reciprocity theorems relate the scattered far field coefficient associated with the scattered cylindrical wave generated by one type of incident wave to the scattered far field coefficient generated by another incident wave; the incident waves here are either plane body or interfacial waves. Typically, one can relate the scattered S field, say, generated by an incident plane P wave to the scattered P field generated by an incident plane S wave; and similarly for the other waves of interest including the interfacial wave. Hence they

provide useful checks upon the numerical analysis, for an obstacle beneath a solid half-space [13] gives the required relations (see also reference [14]). The addition of a fluid overlying the solid leads to some changes; there is now an additional wave due to the fluid half-space and the Schölte wave replaces the Rayleigh wave.

Consider a stress free compact void within the elastic solid, at a finite distance from the interface and with boundary L. The assumption that the obstacle is a stress free void is not necessary for the derivation, but is merely convenient. The results also hold for an obstacle that is a reciprocal linear elastic material either rigidly or smoothly bonded to the surrounding elastic material. In addition, the obstacle can also touch the interface, or one could consider many obstacles a finite distance from the origin. For a void the scattered field within the solid or fluid at a point $\mathbf{x}'$ is given by

$$u_k^{sc}(\mathbf{x}') = \int_L \sigma_{ij,k}^G(\mathbf{x}; \mathbf{x}') u_i^{sc}(\mathbf{x}) n_j \, \mathrm{d}S(\mathbf{x}). \tag{5.1}$$

The integral L is closed if the obstacle is within the solid and open if it touches the boundary. The Green function is given by solutions to equation (3.4), and for a crack equation (5.1) reduces to equation (3.3). The far field in the solid is

$$u_\alpha^{rad}(r, \hat{\mathbf{x}}') = \frac{\mathrm{i}}{4}\left(\frac{2}{\pi k_p r}\right)^{1/2} \exp(\mathrm{i}k_p r - \mathrm{i}\pi/4) P_P(\hat{\mathbf{x}}')\hat{\mathbf{x}}'_\alpha$$

$$+ \varepsilon_{\alpha\gamma 2} \frac{\mathrm{i}}{4}\left(\frac{2}{\pi k_s r}\right)^{1/2} \exp(\mathrm{i}k_s r - \mathrm{i}\pi/4) P_S(\hat{\mathbf{x}}')\hat{\mathbf{x}}'_\gamma \tag{5.2}$$

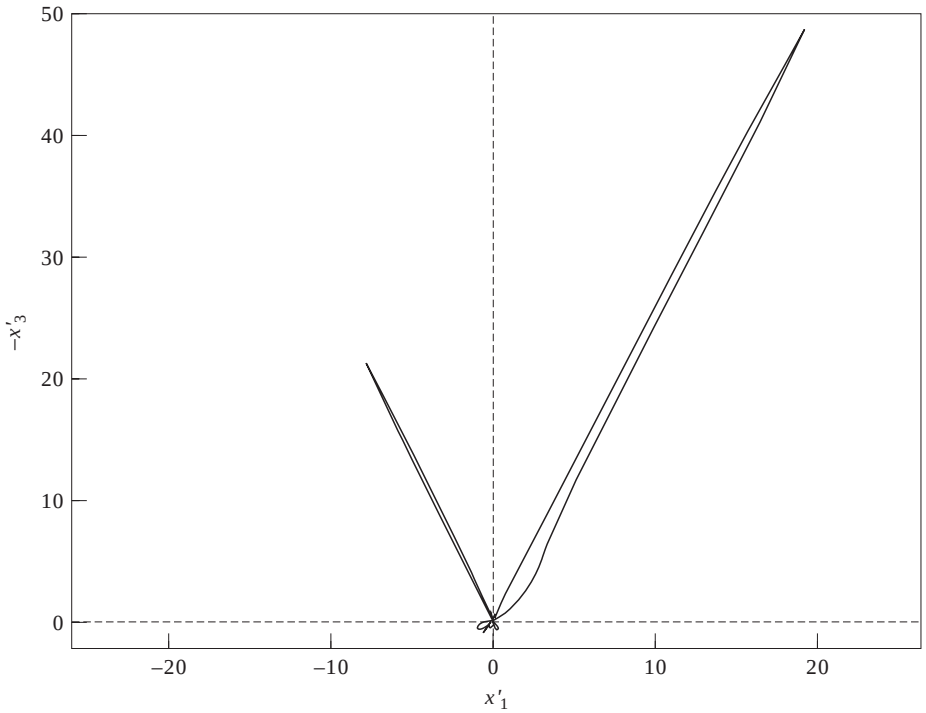

Figure 11. The directivity gains for an incident F wave along $\theta'_i = \pi/4$, $k_s a = 3$, $\varepsilon = 0{\cdot}08$ and $d/a = 0{\cdot}5$ ($P_B = 2{\cdot}3 \times 10^{-2}$). ——, S; ----, P; ——, F.

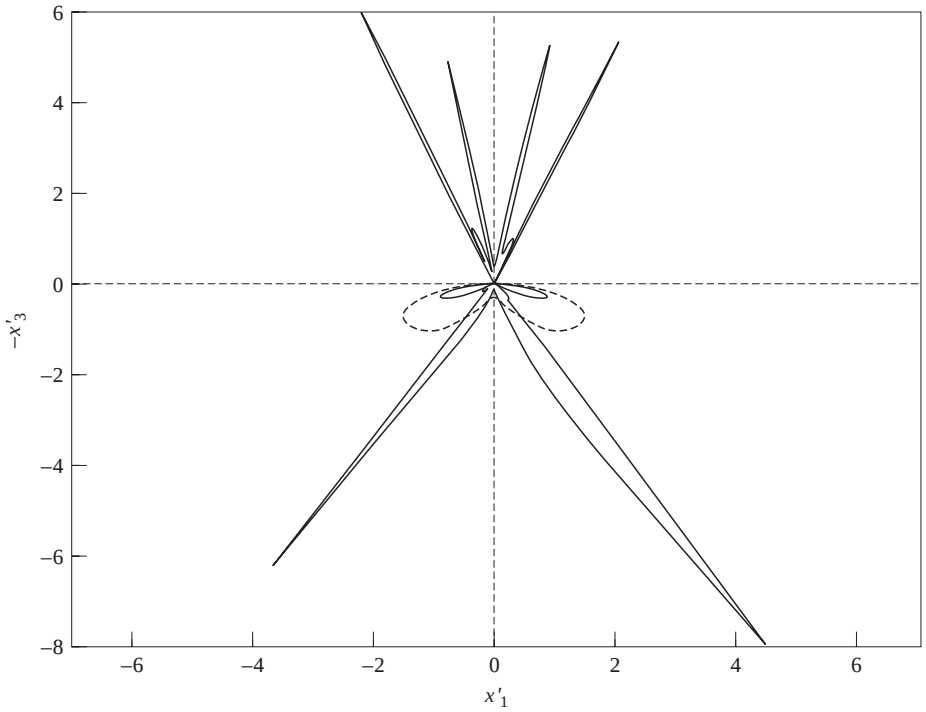

Figure 12. The directivity gains for an incident P wave along $\theta_i = \pi/4$, $k_s a = 3$, $\varepsilon = 0{\cdot}08$ and $d/a = 1{\cdot}5$ ($P_B = 57$). ——, S; ----, P; ——, F.

and in the fluid

$$u_\alpha^{rad}(r, \hat{\mathbf{x}}') = \frac{\mathrm{i}}{4}\left(\frac{2}{\pi k_0 r}\right)^{1/2} \exp(\mathrm{i}k_0 r - \mathrm{i}\pi/4) P_F(\hat{\mathbf{x}}')\hat{\mathbf{x}}'_\alpha, \tag{5.3}$$

where the $P_{P,S,F}(\hat{\mathbf{x}}')$ are the directivity functions. The interfacial Schölte wave in the solid is

$$u_\alpha^{surf}(\mathbf{x}') = H_P^{\pm} k_\alpha^{PSch\pm} \exp(\mathrm{i}k_p \mathbf{k}^{PSch\pm}\cdot\mathbf{x}') + H_S^{\pm}\varepsilon_{\alpha\gamma 2} k_\gamma^{SSch\pm} \exp(\mathrm{i}k_s \mathbf{k}^{Ssch\pm}\cdot\mathbf{x}'); \tag{5.4}$$

there is a similar wave in the fluid. The wavenumber vectors $\mathbf{k}$ are defined in Appendix A. In this paper, surface waves incident from $x_1' = -\infty$ are considered and the superscripts $+$ and $-$ denote the amplitudes travelling in the $+x_1'$ and $-x_1'$ directions respectively. In the absence of the fluid, for incident Rayleigh waves, the above is valid with *Sch* replaced by *R*. The $H_{P,S}$ are the far field amplitudes associated with pieces of the surface wave that could each be associated with P- and S-driven pieces. This split is somewhat unphysical and H_P and H_S are related; thus only results associated with H_P are considered.

Each of the far field directivity functions is defined as an integral over L, such as

$$P_P(\hat{\mathbf{x}}') = \int_L u_\alpha(\mathbf{x})\partial_{\alpha\beta} B_\beta^P(\mathbf{x}; \hat{\mathbf{x}}')\, \mathrm{d}\mathbf{x}, \tag{5.5}$$

with identical expressions for $P_{S,F}$, with S, F replacing P. The far field amplitudes, $H_{P,S}$, also satisfy similar expressions. The function $\partial_{\alpha\beta} B^P_\beta(\mathbf{x}; \hat{\mathbf{x}}')$ is the far field directivity for the stress fields associated with the Green function (see Appendix C). The outward unit normal to the boundary L of the obstacle, that lies in the elastic solid, is $\mathbf{n}$. Using the reciprocal theorem with two independent states, A and B, as scattered fields it is clear that the following identity holds:

$$\int_L u_i^A \sigma_{ij}^{B(in)} n_j \, \mathrm{d}S = \int_L u_i^B \sigma_{ij}^{A(in)} n_j \, \mathrm{d}S. \tag{5.6}$$

Substituting the incident fields due to P, S, F or Schölte waves into this expression, the incident plane P, S or F waves are taken to be in the direction $\mathbf{k} = \hat{\alpha}^{P,S,F}$ in state A and $\mathbf{k} = \hat{\beta}^{P,S,F}$ in state B, with amplitudes A and B respectively, and using the far field expressions the reciprocity relations are found. The directivity functions $P_{P,S,F}(\hat{\mathbf{x}}')$ are written as $G_{P,S,F}(\theta, \phi)$, where the first angle is the angle of incidence associated with the incoming plane wave and the second angle is the angle of observation. For incoming surface waves, the first angle is not required. As the incident waves are taken to be of differing types, a superscript, P, S, F or Sch, is used to denote the type of incident wave. For instance, $G_S^P(\theta, \phi)$ denotes the far field directivity for the scattered cylindrical S wave observed along ϕ and generated by an incident P wave along θ. In the case of incident surface waves, $G_P^{Sch}(\phi)$ denotes the far field directivity for the scattered cylindrical P wave for an incident Schölte wave observed along ϕ.

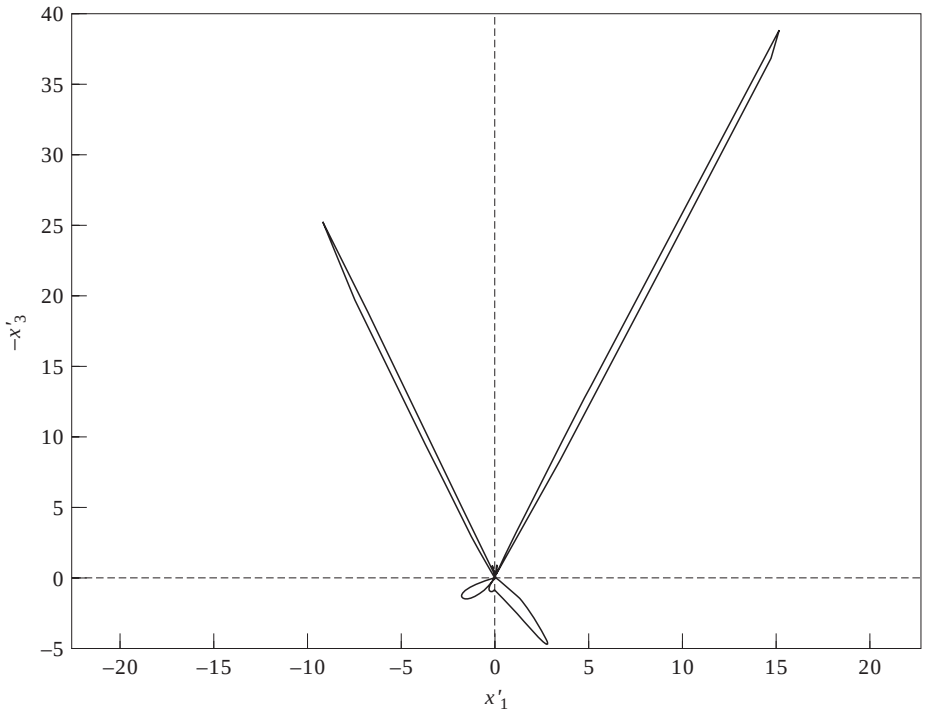

Figure 13. The directivity gains for an incident F wave along $\theta_i' = \pi/4$, $k_s a = 3$, $\varepsilon = 0{\cdot}08$ and $d/a = 1{\cdot}5$ ($P_B = 1{\cdot}6 \times 10^{-3}$). ——, S; ----, P; ——, F.

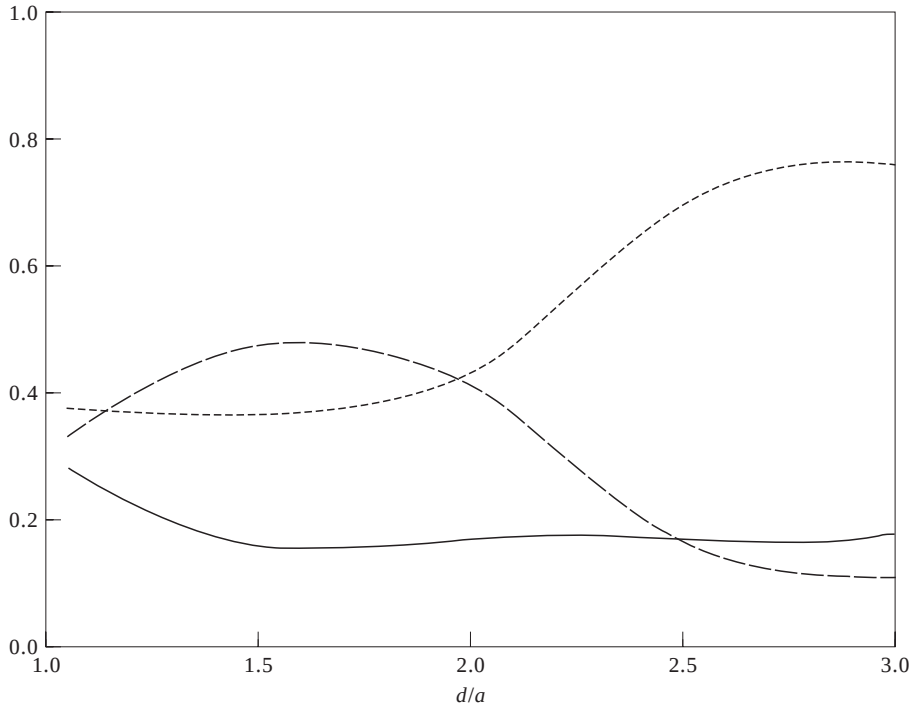

Figure 14. The fraction of scattered power converted to P (——), S (----) and F (——) waves.

For two incident P or S waves, or one incident P wave and one incident S wave, the reciprocity relations are the same as those for an infinite domain [12], and are

$$G_P^p(\theta, \phi) = G_P^p(\phi, \theta), \qquad G_S^S(\theta, \phi) = G_S^S(\phi, \theta), \qquad G_P^S(\theta, \phi) = \frac{k_p^2}{k_s^2} G_S^p(\phi, \theta), \tag{5.7}$$

respectively. These relations are given for incident waves of unit amplitude. Each scattered far field is related to another if each is viewed in the negative direction of the incident direction of propagation of the other.

An incident Schölte wave upon an obstacle generates scattered P, S and F waves. When viewed along an angle α, these are related to the amplitude of the scattered Schölte wave generated by incident plane waves along α. The relations are

$$G_P^{Sch}(\alpha) = \frac{\gamma_p(k)}{(2k_{sch}^2 - k_s^2)^2} \frac{\mathrm{d}S(k)}{\mathrm{d}k}\bigg|_{k = k_{sch}} H_P^{-P}(\alpha), \tag{5.8}$$

$$\frac{k_p^2}{k_s^2} G_S^{Sch}(\alpha) = \frac{\gamma_p(k)}{(2k_{sch}^2 - k_s^2)^2} \frac{\mathrm{d}S(k)}{\mathrm{d}k}\bigg|_{k = k_{sch}} H_P^{-S}(\alpha), \tag{5.9}$$

$$\frac{\varepsilon k_p}{k_0} G_F^{Sch}(\alpha) = \frac{\gamma_p(k)}{(2k_{sch}^2 - k_s^2)^2} \frac{\mathrm{d}S(k)}{\mathrm{d}k}\bigg|_{k = k_{sch}} H_P^{-F}(\alpha). \tag{5.10}$$

The functions $\gamma_p(k)$ and $S(k)$ are defined in Appendix A. Similarly, considering an incident plane F wave and incident F, P and S waves, then

$$G_F^F(\theta, \phi) = G_F^F(\phi, \theta), \qquad \frac{\varepsilon k_p}{k_0} G_F^P(\theta, \phi) = G_P^F(\phi, \theta), \qquad \frac{\varepsilon k_s^2}{k_0 k_p} G_F^S(\theta, \phi) = G_S^F(\phi, \theta). \quad (5.11)$$

The angles in the fluid are given in the same sense as θ_i in Figure 3. The later two relations involve the ratio of densities via ε; recall that $\varepsilon = \rho_f k_p / \rho k_0$.

5.2. POWER FLOW THEOREMS

Another particularly useful application of the reciprocal theorem is to analyze the time averaged power scattered by the crack, and to relate this to a combination of the far field scattering coefficients. As there is no power loss in the material, the total time averaged power flow through a surface S enclosing the obstacle is zero. Thus, utilizing the reciprocal theorem with one state taken to be complex conjugate of the other,

$$\mathrm{Re}\left(\mathrm{i}\omega \int_S \bar{u}_\alpha \sigma_{\alpha\beta} n_\beta \, \mathrm{d}S \right) = 0. \quad (5.12)$$

Taking the surface S to infinity and manipulating the above relation so that it only involves the scattered fields allows the following power balance relations involving the far field directivities and Schölte wave amplitudes to be determined.

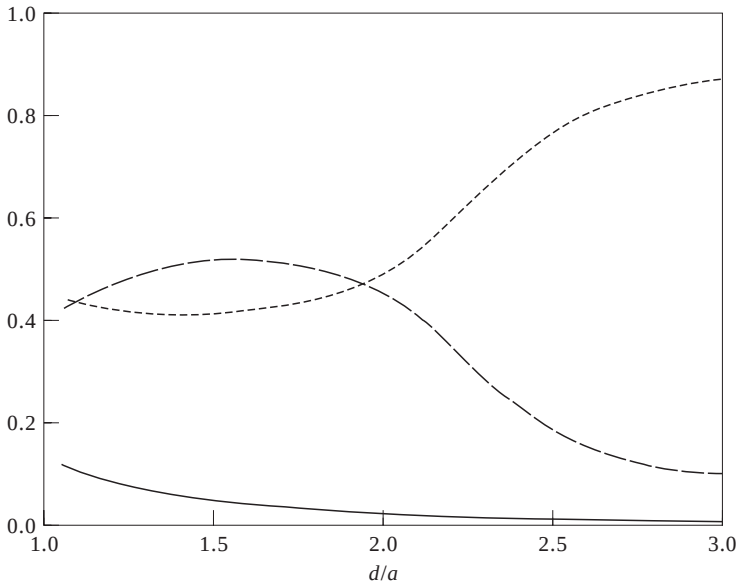

Figure 15. The fraction of scattered power converted to P (——), S (----) and Rayleigh (——) waves.

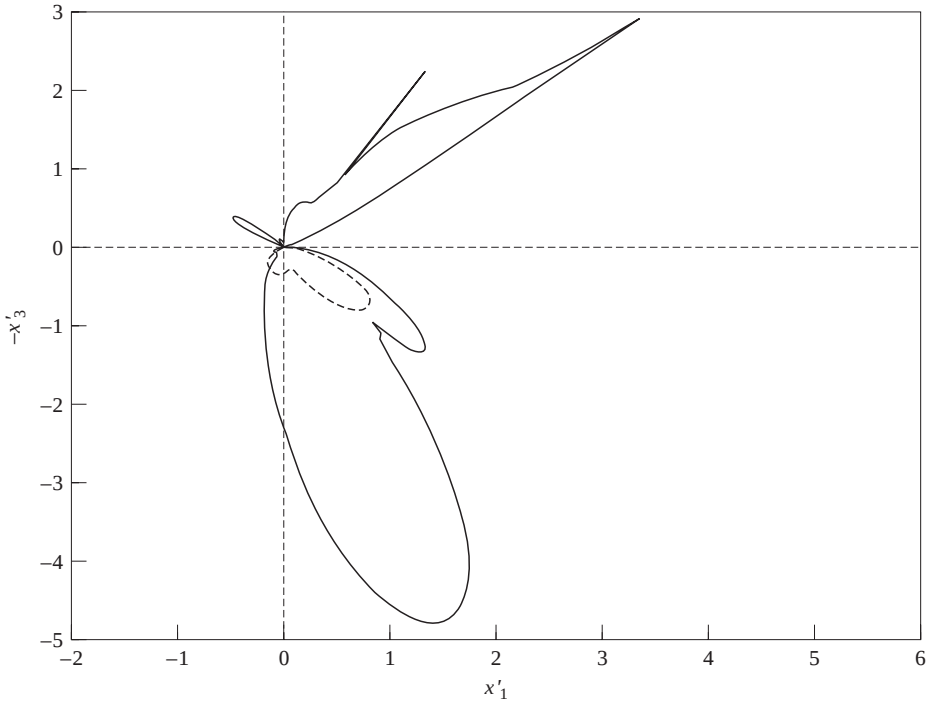

Figure 16. The directivity gains for an incident P wave along $\theta_i = \pi/4$, $k_s a = 3$, $\varepsilon = 0{\cdot}3$ and $d/a = 0{\cdot}5$ ($P_B = 73$). ——, S; ----, P; ——, F.

For an incident P wave,

$$\left(\frac{\omega(\lambda+2\mu)}{16\pi}\int_{-\frac{\pi}{2}}^{\frac{\pi}{2}}|G_P^P(\theta_i,\phi)|^2\,\mathrm{d}\phi+\frac{\omega\mu}{16\pi}\int_{-\frac{\pi}{2}}^{\frac{\pi}{2}}|G_S^P(\theta_i,\phi)|^2\,\mathrm{d}\phi+\frac{\omega\lambda_f}{16\pi}\int_{-\frac{\pi}{2}}^{\frac{\pi}{2}}|G_F^P(\theta_i,\phi')|^2\,\mathrm{d}\phi'\right)$$

$$+\left(\frac{\mathrm{i}\omega(\lambda+2\mu)}{4}\frac{S'(k)\gamma_p}{(2k^2-k_s^2)^2}\bigg|_{k=k_{sch}}(|H_P^{-P}(\theta_i)|^2+|H_P^{+P}(\theta_i)|^2)\right)$$

$$=\frac{\omega}{2}\,\mathrm{Im}\,((\lambda+2\mu)R_{PP}G_P^P(\theta_i,-\theta_i)+\mu R_{SP}G_S^P(\theta_i,-\theta_s^p)+\lambda_f T_{FP}G_F^P(\theta_i,-\theta_f^p))|_{k=k_p\sin\theta_i}, \tag{5.13}$$

where $k_s \sin\theta_s^p = k_p \sin\theta_i$ and $k_0 \sin\theta_f^p = k_p \sin\theta_i$. The reflection and transmission coefficients are defined in Appendix A. The top line of equation (5.13) is the body wave contribution to the time averaged scattered power, P_{body} in equations (4.1) and (4.2), and each integral represents the power converted to cylindrical P, S and F waves respectively. The next term represents the surface wave contribution. These are, perhaps surprisingly, related to a combination of the far field scattering coefficients. The coefficients in the combination of the far field scattering coefficients are related to the reflection and transmission coefficients for an incident plane P wave on the interface. These relations allow us to evaluate the proportion of the total scattered time averaged power that is converted into each type of wave. In the absence of the fluid, and after setting $k_{sch} = k_r$ in the above, the results found in reference [13] are recovered; see also Gregory [23]. For $\varepsilon = 0$, the terms on the right side of equation (5.13) are the analytical continuation of $\mathrm{Im}\,(G_P^P(\theta_i, -\theta_i'))$ in reference [13]—that is, where θ_i' is in the fluid—into the physical domain.

Similarly, one can deduce for an incident S wave that

$$\left(\frac{\omega(\lambda+2\mu)}{16\pi}\int_{-\frac{\pi}{2}}^{\frac{\pi}{2}}|G_P^S(\theta_i,\phi)|^2\,\mathrm{d}\phi+\frac{\omega\mu}{16\pi}\int_{-\frac{\pi}{2}}^{\frac{\pi}{2}}|G_S^S(\theta_i,\phi)|^2\,\mathrm{d}\phi+\frac{\omega\lambda_f}{16\pi}\int_{-\frac{\pi}{2}}^{\frac{\pi}{2}}|G_F^S(\theta_i,\phi')|^2\,\mathrm{d}\phi'\right)$$
$$+\left(\frac{\mathrm{i}\omega(\lambda+2\mu)}{4}\frac{S'(k)\gamma_p}{(2k^2-k_s^2)^2}\bigg|_{k=k_{sch}}(|H_P^{-S}(\theta_i)|^2+|H_P^{+S}(\theta_i)|^2)\right)$$
$$=\frac{\omega}{2}\,\mathrm{Im}\,((\lambda+2\mu)R_{PS}G_P^S(\theta_i,-\theta_p^s)+\mu R_{SS}G_S^S(\theta_i,-\theta_i)+\lambda_f T_{FS}G_F^S(\theta_i,-\theta_f^s))|_{k=k_s\sin\theta_i}, \tag{5.14}$$

where $k_p\sin\theta_p^s=k_s\sin\theta_i$ and $k_0\sin\theta_f^s=k_s\sin\theta_i$; for some angles of incidence the angle θ_p^s is complex. For an incident F wave, the power balance is

$$\left(\frac{\omega(\lambda+2\mu)}{16\pi}\int_{-\frac{\pi}{2}}^{\frac{\pi}{2}}|G_P^F(\theta_i,\phi)|^2\,\mathrm{d}\phi+\frac{\omega\mu}{16\pi}\int_{-\frac{\pi}{2}}^{\frac{\pi}{2}}|G_S^F(\theta_i,\phi)|^2\,\mathrm{d}\phi+\frac{\omega\lambda_f}{16\pi}\int_{-\frac{\pi}{2}}^{\frac{\pi}{2}}|G_F^F(\theta_i,\phi')|^2\,\mathrm{d}\phi'\right)$$
$$+\left(\frac{\mathrm{i}\omega(\lambda+2\mu)}{4}\frac{S'(k)\gamma_p}{(2k^2-k_s^2)^2}\bigg|_{k=k_{sch}}(|H_P^{-F}(\theta_i)|^2+|H_P^{+F}(\theta_i)|^2)\right)$$
$$=\frac{\omega}{2}\,\mathrm{Im}\,((\lambda+2\mu)T_{PF}G_P^F(\theta_i,-\theta_p^f)+\mu T_{SF}G_S^F(\theta_i,-\theta_s^f)+\lambda_f R_{FF}G_F^F(\theta_i,-\theta_i))|_{k=k_0\sin\theta_i}, \tag{5.15}$$

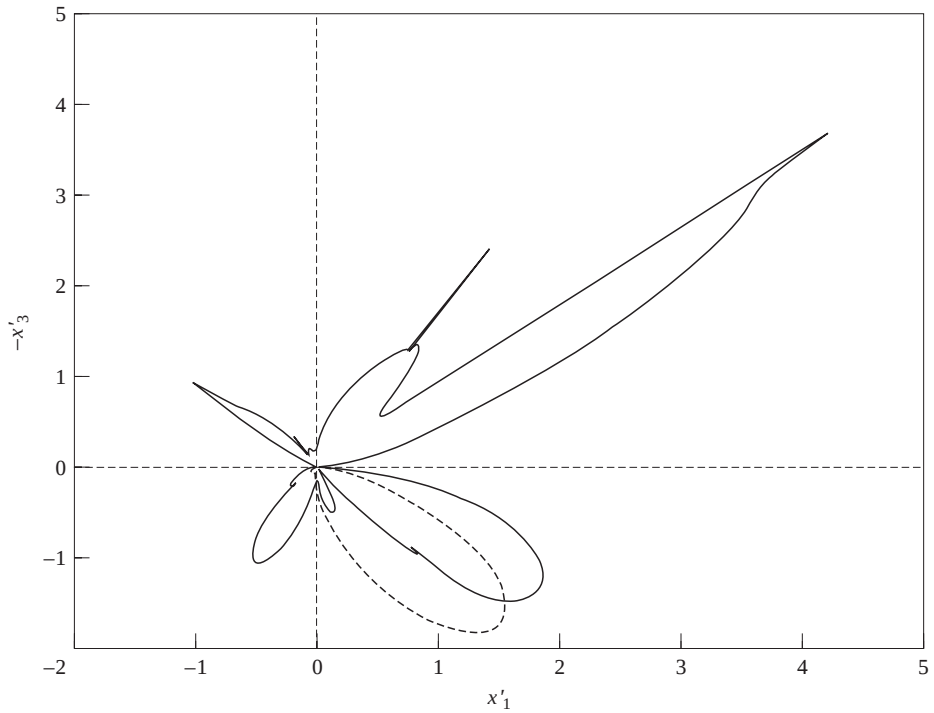

Figure 17. The directivity gains for an incident F wave along $\theta_i'=\pi/4$, $k_sa=3$, $\varepsilon=0{\cdot}3$ and $d/a=0{\cdot}5$ ($P_B=14$). ——, S; ----, P; ——, F.

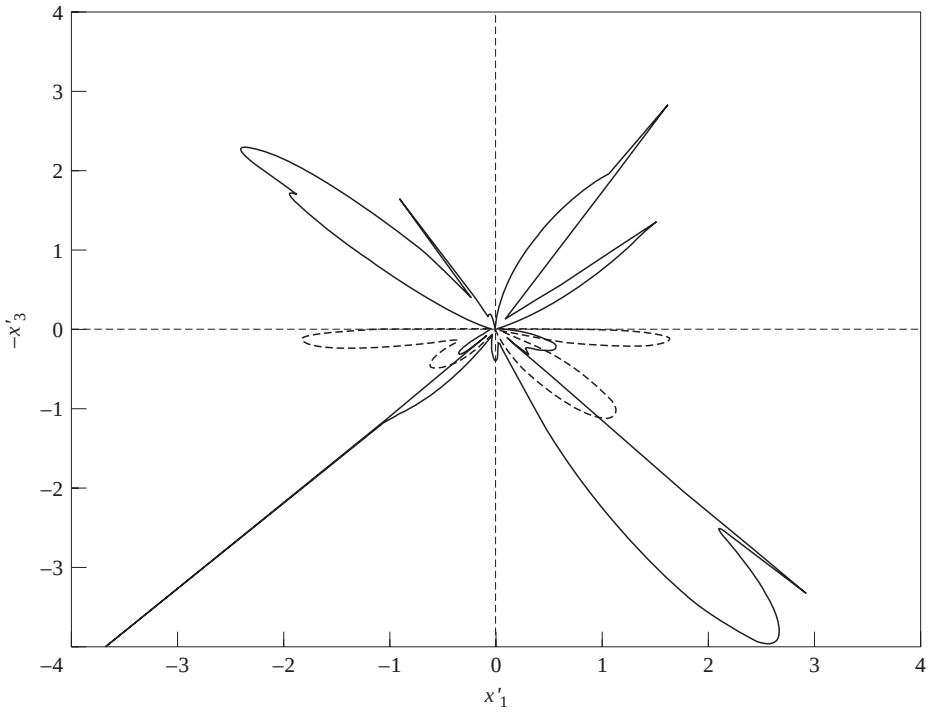

Figure 18. The directivity gains for an incident P wave along $\theta_i = \pi/4$, $k_s a = 3$, $\varepsilon = 0{\cdot}3$ and $d/a = 1{\cdot}5$ ($P_B = 50$). ——, S; ----, P; ——, F.

where $k_p \sin\theta_p^f = k_0 \sin\theta_i$ and $k_s \sin\theta_s^f = k_0 \sin\theta_i$; both angles θ_p^f and θ_s^f are complex for some angles of incidence. For an incident Schölte wave,

$$\left(\frac{\omega(\lambda+2\mu)}{16\pi}\int_{-\frac{\pi}{2}}^{\frac{\pi}{2}} |G_P^{Sch}(\theta_i,\phi)|^2\,\mathrm{d}\phi + \frac{\omega\mu}{16\pi}\int_{-\frac{\pi}{2}}^{\frac{\pi}{2}} |G_S^{Sch}(\theta_i,\phi)|^2\,\mathrm{d}\phi\right.$$

$$\left. + \frac{\omega\lambda_f}{16\pi}\int_{-\frac{\pi}{2}}^{\frac{\pi}{2}} |G_F^{Sch}(\theta_i,\phi')|^2\,\mathrm{d}\phi'\right) + \left(\frac{\mathrm{i}\omega(\lambda+2\mu)}{4}\frac{S'(k)\gamma_p}{(2k^2-k_s^2)^2}\bigg|_{k=k_{sch}}(|T|^2+|R|^2-1)\right) = 0. \tag{5.16}$$

The transmission and reflection coefficients for Schölte waves are $H_P^{+Sch} = T - 1$ and $H_P^{-Sch} = R$. The power balance relations are a particularly useful check, as they relate the integral of the directivities to the scattered directivities along a ray.

Both the reciprocity and power flow theorems were used as a check upon the numerical results presented in earlier sections.

A note of warning regarding both reciprocal and power flow theorems as a check upon numerical calculations is worth emphasizing. These theorems do not necessarily provide an accurate check upon how well a physical problem is solved. The numerical approach utilized above satisfies reciprocity and the power balance analytically.

As an example, consider the scattering of incident plane waves by a finite length crack in an infinite elastic medium and solve the integral equations by using an expansion of the unknowns in a sequence of N Chebyshev polynomials; cf. reference [11]. For $k_s a = 3$ and $v = \frac{1}{3}$, a relative accuracy of $O(10^{-4})$ in the calculation for the stress intensity factors due to an incident P wave is achieved using $N = 8$ and $N = 10$; for $N = 8$ the power flow

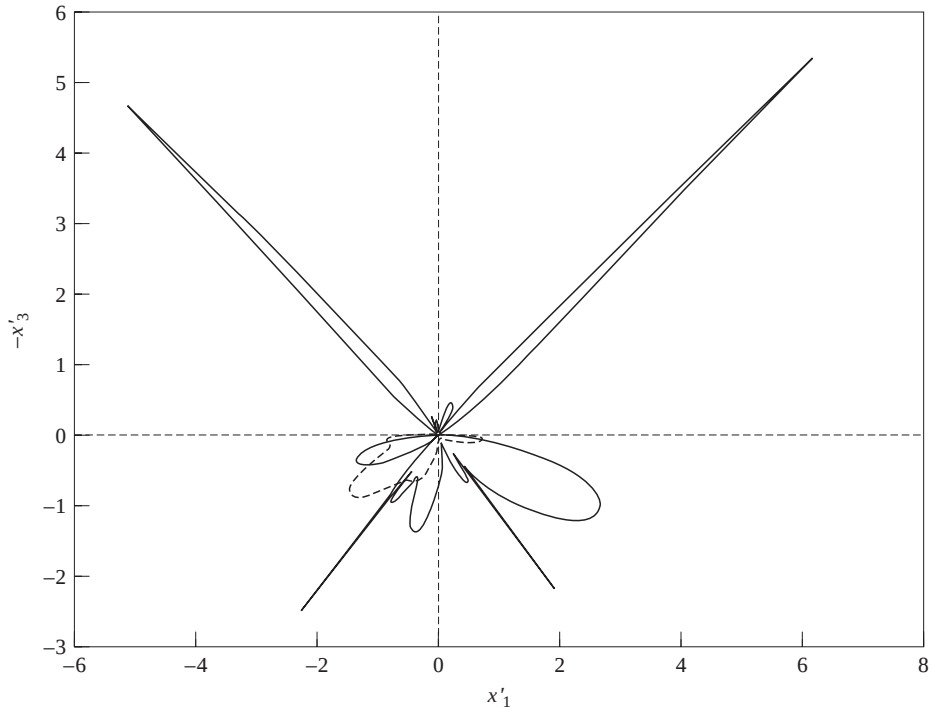

Figure 19. The directivity gains for an incident F wave along $\theta_i' = \pi/4$, $k_s a = 3$, $\varepsilon = 0{\cdot}3$ and $d/a = 1{\cdot}5$ ($P_B = 23$). ——, S; ----, P; ——, F.

calculation is accurate to $O(10^{-6})$, with no difference in the functions related via reciprocity due to differing incident fields. However, if one takes, say, $N = 2$, the calculated stress intensity factors are up to twice that evaluated at $N = 8$, but the power flow and reciprocity relations are still satisfied to the same accuracy as before! Thus the power flow and reciprocity relations are an internal consistency check upon a numerical procedure, but do not provide a completely independent check upon the accuracy to which the physical problem is solved.

6. CONCLUSIONS

The wave–crack interaction problem for an arbitrarily orientated crack is solved using an efficient numerical procedure. The formulation and analysis is for a single crack in an infinite elastic half-space. Material parameters have been chosen to be typical of metal–water and rock–water interfaces, thus representing light and moderate fluid coupling, and a variety of results are presented. In this paper results are presented for cracks either parallel to, or perpendicular to, the interface. The main results are as follows.

1. The stress intensity factors for incident waves from the solid, in the limit of light fluid loading, are not changed substantially from those found in the absence of the fluid. For an incident plane wave from the fluid, large responses are found when the angle of incidence is the Rayleigh angle, suggesting that considerable wave–crack interaction occurs for waves incident along the Rayleigh angle.

2. The far field scattering directivities are analyzed and it is shown that there are effectively two regimes. In the light fluid coupling case, beam formation along the Rayleigh angles is dominant. As the coupling increases, other beams are formed along critical angles associated with head waves. For sufficiently large coupling, these then become dominant.

3. Reciprocity and power flow theorems are deduced and these are used as checks upon the numerical work. In addition, the power flow results allow the partition of the scattered power into its constituent parts to be analyzed. For waves incident from the fluid, a considerable proportion of the scattered power is converted to scattered waves in the fluid and in general very little is converted to Schölte waves.

ACKNOWLEDGMENTS

The financial support of an EPSRC Advanced Fellowship is gratefully acknowledged, as is the support of the Nuffield Foundation.

REFERENCES

1. D. A. Mendelsohn, J. D. Achenbach and L. M. Keer 1980 *Wave Motion* **2**, 277–292. Scattering of elastic waves by a surface breaking crack.
2. J. D. Achenbach, W. Lin and L. M. Keer 1983 *IEEE Transactions on Sonics and Ultrasonics* **30**, 270–276. Surface waves due to scattering by a near-surface parallel crack.
3. R. J. Brind and J. D. Achenbach 1981 *Journal of Sound and Vibration* **78**, 555–563. Scattering of longitudinal and transverse waves by a sub-surface crack.
4. J. H. M. T. van der Hijden and F. L. Neerhoff 1984 *Journal of the Acoustical Society of America* **75**, 1694–1704. Diffraction of elastic waves by a sub-surface crack (in-line motion).
5. L. M. Keer, W. Lin and J. D. Achenbach 1984 *Transactions of the American Society of Mechanical Engineers*, *Journal of Applied Mathematics* **51**, 65–70. Resonance effects for a crack near a free surface.
6. J. H. M. T. van der Hijden and F. L. Neerhoff 1985 *Proceedings of the IEEE Symposium*. Reflection and transmission of surface acoustic waves by a near-surface crack of arbitrary orientation.
7. S. M. Gracewski and D. B. Bogy 1986 *Transactions of the American Society of Mechanical Engineers*, *Journal of Applied Mechanics* **53**, 326–332. Elastic wave scattering from an interface crack in a layered half space submerged in water, part 1: applied tractions at the liquid–solid interface.
8. V. S. Ahn, J. G. Harris and J. D. Achenbach 1992 *IEEE Transactions on Ultrasonics Ferroelectrics and Frequency Control* **39**, 112–118. Numerical analysis of the acoustic signature of a surface breaking crack.
9. F. L. Neerhoff 1979 *Applied Science Research* **35**, 237–249. Diffraction of Love waves by a stress-free crack of finite width in the plane interface of a layered composite.
10. F. L. Neerhoff and J. H. M. T. van der Hijden 1984 *Journal of Sound and Vibration* **93**, 523–536. Diffraction of elastic waves by a sub-surface crack (anti-plane motion).
11. J. H. M. T. van der Hijden and F. L. Neerhoff 1984 *Transactions of the American Society of Mechanical Engineers*, *Journal of Applied Mechanics* **51**, 646–651. Scattering of elastic waves by a plane crack of finite width.
12. T. H. Tan 1977 *Journal of the Acoustical Society of America* **61**, 928–931. Reciprocity relations for scattering of plane, elastic waves.
13. F. L. Neerhoff 1980 *Wave Motion* **2**, 99–113. Reciprocity and power-flow theorems for the scattering of plane elastic waves in a half space.
14. C. C. Mei 1978 *Journal of the Acoustical Society of America* **64**, 1514–1522. Extensions of some identities in elastodynamics with rigid inclusions.
15. Z. M. Rogoff 1993 *M.Sc. Thesis*, *University of Manchester*. Reciprocity relations between the incident field and mode-converted scattered far field for compact obstacles in an elastic half space.
16. M. L. Williams 1957 *Transactions of the American Society of Mechanical Engineers*, *Journal of Applied Mechanics* **24**, 109–114. The stress distribution at the base of a stationary crack.
17. R. H. Tew 1992 *Proceedings of the Royal Society of London* **A437**, 433–449. Non-specular reflection phenomena at a fluid-solid boundary.
18. G. A. D. Briggs 1992 *Acoustic Microscopy*. Oxford: Oxford University Press.
19. L. M. Brekhovskikh 1980 *Waves in Layered Media*. New York: Academic Press; second edition.
20. R. V. Craster 1996 *Quarterly Journal of Mechanics and Applied Mathematics* **49**, 657–674. Wavefront expansions for pulse scattering by a surface inhomogeneity.

21. G. C. Sih and H. Liebowitz 1968 In *Fracture, an Advanced Treatise*, Vol. 2 (H. Liebowitz, editor). New York: Academic Press. Mathematical theories of brittle fracture.
22. R. V. Craster 1997 *European Journal of Applied Mathematics*, to appear. The light fluid loading limit for fluid/solid interactions.
23. R. D. Gregory 1974 *Mathematical Proceedings of the Cambridge Philosophical Society* **77**, 385–404. The non-existence of standing waves in certain problems of linear elasticity.
24. R. V. Craster 1996 *Proceedings of the Royal Society of London* **A452**, 1695–1711. A canonical problem for fluid–solid interfacial wave coupling.
25. S. K. Lucas 1995 *Journal of Computational Applied Mathematics* **64**, 269–282. Evaluating infinite integrals involving products of Bessel functions of arbitrary order.

APPENDIX A: TRANSFORM DEFINITIONS USED IN THE TEXT

$$\gamma_q(k) = (k_q^2 - k^2)^{1/2} \qquad \text{for } q = d, s, 0,$$

$$R(k) = 4k^2\gamma_s(k)\gamma_p(k) + (2k^2 - k_s^2)^2,$$

$$S(k) = 4k^2\gamma_s(k)\gamma_p(k) + \frac{\varepsilon k_0\gamma_p k_s^4}{k_p\gamma_0} + (2k^2 - k_s^2)^2,$$

$$V = -\frac{2k\gamma_p k_s}{k_p(2k^2 - k_s^2)}, \qquad V_f = -\frac{k_s^2\gamma_p k_0}{k_p\gamma_0(2k^2 - k_s^2)}.$$

Reflection and transmission functions:

$$R_{PP}S(k) = 4k^2\gamma_s(k)\gamma_p(k) + \frac{\varepsilon k_0\gamma_p k_s^4}{k_p\gamma_0} - (2k^2 - k_s^2)^2,$$

$$R_{PS}S(k) = -4k\gamma_s k_p(2k^2 - k_s^2)/k_s, \qquad R_{SP}S(k) = 4k\gamma_p k_s(2k^2 - k_s^2)/k_p,$$

$$R_{SS}S(k) = 4k^2\gamma_s(k)\gamma_p(k) - \frac{\varepsilon k_0\gamma_p k_s^4}{k_p\gamma_0} - (2k^2 - k_s^2)^2,$$

$$R_{FF}S(k) = 4k^2\gamma_s(k)\gamma_p(k) - \frac{\varepsilon k_0\gamma_p k_s^4}{k_p\gamma_0} + (2k^2 - k_s^2)^2,$$

$$T_{FS}S(k) = -4kk_s k_0\gamma_s\gamma_p/\gamma_0, \qquad T_{SF}S(k) = 4\varepsilon k k_s^3\gamma_p/k_p,$$

$$T_{FP}S(k) = -2\gamma_p k_s^2 k_0(2k^2 - k_s^2)/k_p\gamma_0, \qquad T_{PF}S(k) = -2\varepsilon(2k^2 - k_s^2)k_s^2.$$

The wavenumber vectors:

$$\mathbf{k}^F = \frac{1}{k_0}(k, \gamma_0), \qquad \mathbf{k}^{FF} = \frac{1}{k_0}(k, -\gamma_0), \qquad \mathbf{k}^{PF} = \frac{1}{k_p}(k, \gamma_p), \qquad \mathbf{k}^{SF} = \frac{1}{k_s}(k, \gamma_s),$$

$$\mathbf{k}^P = \frac{1}{k_p}(k, -\gamma_p), \qquad \mathbf{k}^{PP} = \frac{1}{k_p}(k, \gamma_p), \qquad \mathbf{k}^{SP} = \frac{1}{k_s}(k, \gamma_s), \qquad \mathbf{k}^{PSch\pm} = \frac{1}{k_p}(k, \gamma_p)|_{k = \pm k_{sch}},$$

$$\mathbf{k}^S = \frac{1}{k_s}(k, -\gamma_s), \qquad \mathbf{k}^{SS} = \frac{1}{k_s}(k, \gamma_s), \qquad \mathbf{k}^{PS} = \frac{1}{k_p}(k, \gamma_p), \qquad \mathbf{k}^{SSch\pm} = \frac{1}{k_s}(k, \gamma_s)|_{k = \pm k_{sch}}.$$

APPENDIX B: KERNEL FUNCTIONS

The rotation from the $\mathbf{x}'$ into the $\mathbf{x}$ co-ordinate system introduces the crack inclination angle θ into the transform representations of the Green function when it is used in the integral equations. A concise notation is $k^{\pm} = k\cos\theta \pm \gamma\sin\theta$, $\gamma^{\pm} = \gamma\cos\theta \mp k\sin\theta$. In

addition, the notation $C_1^{p\pm} = \mp 2k_p^{\pm}\gamma_p^{\pm}$, $C_3^{p\pm} = k_s^2 - 2(k_p^{\pm})^2$ and $C_1^{s\pm} = (k_s^{\pm})^2 - (\gamma_s^{\pm})^2$, $C_3^{s\pm} = \mp 2k_s^{\pm}\gamma_s^{\pm}$ is also used. The kernel functions are deduced to be

$$K_{\alpha\beta;mn} = (-1)^{m+n} \int_C L_{\alpha\beta;mn}(k)/k_s^2 \, \mathrm{d}k,$$

where

$$\begin{aligned} L_{\alpha\beta;mn}(k) = {} & \delta_{\alpha\beta} R(k) \frac{\mathrm{J}_m(ka)\mathrm{J}_n(ka)}{\gamma_\alpha k^2} \\ & + \frac{R_{PP} C_\alpha^{p+} C_\beta^{p-}}{\gamma_p k_p^+ k_p^-} \mathrm{J}_m(ak_p^+)\mathrm{J}_n(ak_p^-)\, \mathrm{e}^{2\mathrm{i}\gamma_p d} + \frac{R_{SS} C_\alpha^{s+} C_\beta^{s-}}{\gamma_s k_s^+ k_s^-} \mathrm{J}_m(ak_s^+)\mathrm{J}_n(ak_s^-)\, \mathrm{e}^{2\mathrm{i}\gamma_s d} \\ & + \left(\frac{k_p R_{SP} C_\alpha^{p+} C_\beta^{s-}}{k_s \gamma_p k_p^+ k_s^-} \mathrm{J}_m(ak_p^+)\mathrm{J}_n(ak_s^-) + \frac{k_s R_{PS} C_\alpha^{s+} C_\beta^{p-}}{k_p \gamma_s k_s^+ k_p^-} \mathrm{J}_m(ak_s^+)\mathrm{J}_n(ak_p^-) \right) \mathrm{e}^{\mathrm{i}(\gamma_p + \gamma_s)d}, \end{aligned}$$

where $\gamma_{1,3} = \gamma_{s,p}$. The path C runs from $-\infty$ to $+\infty$ and is indented to lie beneath the pole and branch points that lie on the positive real axis and above those on the negative real axis. Superficially, they are identical to the kernel functions derived in reference [4], (as an aside, this will always be the case for cracks beneath plane solid/solid interfaces—the only change is in the definition of the reflection terms); however, there is a crucial difference. The denominator that appears within the reflection coefficients is $S(k)$ rather than $R(k)$. The former contains six branch points and either two or four zeros depending upon the precise choice of branch cuts (see the appendix of Craster [24]): the latter has four branch points and two real zeros. Here the choice of cuts in the upper half-plane is taken such that they run from $+k_{p,s,0}$ to $+k_{p,s,0} + \mathrm{i}\infty$, with a similar choice for the lower branch cut. Thus the analysis is slightly more involved than that required in the absence of the fluid, the pole contribution on the real axis is explicitly evaluated and subtracted from the integrand. For $\varepsilon \ll 1$ the contribution due to the leaky pole is similarly subtracted; this only becomes necessary for $\varepsilon \sim 0{\cdot}01$. The remaining integrand is manipulated so that it runs from zero to infinity and is split into finite pieces from one branch point to another and finally out to infinity. Each piece is manipulated so that no branch point singularities remain explicitly within the integrand and then standard numerical techniques—here Gaussian quadrature with 31 or 51 nodes—yield fast and accurate solutions. This is considerably faster than deforming the contour around the branch points and integrating numerically in the complex domain. The Bessel functions are evaluated using an integral representation: this was found to be faster and more accurate than using recurrence relation based methods. The Bessel function products in the integrand might appear to introduce awkward oscillatory behaviour, and techniques designed specifically for such integrals can be utilized (Lucas [25]). On some integrals this did improve the speed of calculation; however, the evaluation time is already so short that the extra effort of programming in these faster methods was not warranted and conventional techniques suffice. If the crack is either parallel to, or perpendicular to, the interface then considerable simplifications occur, in addition natural symmetries emerge; thus in these cases the numerical approach becomes even more efficient.

APPENDIX C: THE GREEN'S STATE

In the text the Green's state associated with $\sigma_{kj,j}^G(\mathbf{x};\mathbf{p}) + \rho\omega^2 u_k^G(\mathbf{x};\mathbf{p}) = -\delta(\mathbf{x}-\mathbf{p})$ is required in $x_3' > 0$. The displacements $u_{i,k}^G(\mathbf{x}',\mathbf{p}')$ are $u_{i,k}^{G\infty}(\mathbf{x}',\mathbf{p}') + u_{i,k}^{GI}(\mathbf{x}',\mathbf{p}')$, where the first

term is the usual elastic Green function in an infinite domain and the second term takes account of the interface, and is

$$u^{GI}_{\alpha;\beta}(\mathbf{x}', \mathbf{p}') = \frac{\mathrm{i}}{4\pi\mu}\int_{-\infty}^{\infty} \frac{k_p^2}{k_s^2\gamma_p}\,(k_\alpha^{PP}R_{PP}\,\mathrm{e}^{\mathrm{i}k_p\mathbf{k}^{PP}\mathbf{x}'} + \varepsilon_{\alpha\beta\gamma}R_{SP}k_\gamma^{SP}\,\mathrm{e}^{\mathrm{i}k_s\mathbf{k}^{SP}\mathbf{x}'})k_\beta^P\,\mathrm{e}^{-\mathrm{i}k_p\mathbf{k}^P\mathbf{p}'}\,\mathrm{d}k$$

$$+\frac{1}{\gamma_s}\,(\varepsilon_{\alpha\gamma 2}k_\gamma^{SS}R_{SS}\,\mathrm{e}^{\mathrm{i}k_s\mathbf{k}^{SS}\mathbf{x}'} + k_\alpha^{PS}R_{PS}\,\mathrm{e}^{\mathrm{i}k_p\mathbf{k}^{PS}\mathbf{x}'})\,\mathrm{e}^{-\mathrm{i}k_s\mathbf{k}^S\mathbf{p}'}\varepsilon_{\beta\gamma 2}k_\gamma^S\,\mathrm{d}k. \tag{C.1}$$

The wavenumber vectors are given in Appendix A. For the integral equation we require the Green functions relative to the **x** co-ordinate system: these are found by determining the potential representations for point forces in the $1', 3'$ directions and then rotating on to the 1, 3 system, thus determining the potential representations due to point forces in the 1, 3 directions. Hence in the solid one finds equation (B2) of reference [4] with the reflection functions replaced by those of Appendix A of the present paper. In the fluid,

$$\sigma^{GI}_{\alpha 3}(x_1, x_3; p_1, p_3) = -\mu k_0/2\rho_f\omega^2,$$

$$\left(\frac{T_{PF}}{k_p}\,C_\alpha^{p-}\,\mathrm{e}^{\mathrm{i}((\gamma_p+\gamma_0)d + x_1k_p^- + x_3\gamma_p^-)} + \frac{T_{SF}}{k_s}\,C_\alpha^{s-}\,\mathrm{e}^{\mathrm{i}((\gamma_s+\gamma_0)d + x_1k_s^- + x_3\gamma_s^-)}\right). \tag{C.2}$$

The far field is

$$u^{G(rad)}_{\alpha;\beta}(\mathbf{x}, r, \hat{\mathbf{x}}') = \frac{\mathrm{i}}{4}\left(\frac{2}{\pi k_p r}\right)^{1/2}\exp(\mathrm{i}k_p r - \mathrm{i}\pi/4)B_\alpha^P(\mathbf{x}, \hat{\mathbf{x}}')\hat{\mathbf{x}}'_\beta$$

$$+\,\varepsilon_{\beta\gamma 2}\frac{\mathrm{i}}{4}\left(\frac{2}{\pi k_s r}\right)^{1/2}\exp(\mathrm{i}k_s r - \mathrm{i}\pi/4)B_\alpha^S(\mathbf{x}, \hat{\mathbf{x}}')\hat{\mathbf{x}}'_\gamma \tag{C.3}$$

for $k_{p,s}r \gg 1$, and

$$u^{rad}_\alpha(\mathbf{x}, r, \hat{\mathbf{x}}') = \frac{\mathrm{i}}{4}\left(\frac{2}{\pi k_0 r}\right)^{1/2}\exp(\mathrm{i}k_0 r - \mathrm{i}\pi/4)B_\alpha^F(\mathbf{x}, \hat{\mathbf{x}}')\hat{\mathbf{x}}'_3. \tag{C.4}$$

The far field cylindrical wave in the fluid only becomes fully developed in the light fluid loading limit for $k_0 r \gg 1/\varepsilon^2$; there is interesting non-uniform behaviour in the neighbourhood of the Rayleigh angle for $1 \ll k_0 r \ll 1/\varepsilon^2$ [17].

The $B_\alpha^{P,S,F}(\mathbf{x}, \hat{\mathbf{x}}')$ are given by

$$B_\alpha^F(\mathbf{x}, \hat{\mathbf{x}}') = -\frac{1}{\lambda_f}\,(x_\alpha^{PF}T_{PF}\,\mathrm{e}^{\mathrm{i}k_p\hat{\mathbf{x}}_{PF}\cdot\mathbf{x}} + \varepsilon_{\alpha\gamma 2}x_\gamma^{SF}T_{SF}\,\mathrm{e}^{\mathrm{i}k_s\hat{\mathbf{x}}_{SF}\cdot\mathbf{x}}), \tag{C.5}$$

$$B_\alpha^P(\mathbf{x}, \hat{\mathbf{x}}') = (\lambda+2\mu)^{-1}(\hat{x}'_\alpha\,\mathrm{e}^{-\mathrm{i}k_p\hat{\mathbf{x}}'\cdot\mathbf{x}} - \hat{x}_\alpha'^{PP}R_{PP}\,\mathrm{e}^{\mathrm{i}k_p\hat{\mathbf{x}}'^{PP}\cdot\mathbf{x}} - \varepsilon_{\alpha\gamma 2}\hat{x}_\gamma'^{SP}R_{SP}\,\mathrm{e}^{\mathrm{i}}k_s\hat{\mathbf{x}}'^{SP}\cdot\mathbf{x}), \tag{C.6}$$

$$B_\alpha^S(\mathbf{x}, \hat{\mathbf{x}}') = \mu^{-1}(\varepsilon_{\alpha\gamma 2}\hat{x}'_\gamma\,\mathrm{e}^{-\mathrm{i}k_s\hat{\mathbf{x}}'\cdot\mathbf{x}} - \varepsilon_{\alpha\gamma 2}\hat{x}_\gamma'^{SS}R_{SS}\,\mathrm{e}^{\mathrm{i}k_s\hat{\mathbf{x}}'^{SS}\cdot\mathbf{x}} - \hat{x}_\alpha'^{PS}R_{PS}\,\mathrm{e}^{\mathrm{i}k_p\hat{\mathbf{x}}'^{PS}\cdot\mathbf{x}}), \tag{C.7}$$

with the $\hat{\mathbf{x}}'$ as the geometrical counterparts of the wavenumber vectors in Appendix A.

APPENDIX D: INCIDENT AND SCATTERED FIELDS

For an incident P wave with amplitude A_p, the incident field in the solid is

$$u_\alpha^{in}(\mathbf{x}') = A_\alpha^P\,\mathrm{e}^{\mathrm{i}k_p\mathbf{k}^P\cdot\mathbf{x}'} + A_\alpha^{PP}\,\mathrm{e}^{\mathrm{i}k_p\mathbf{k}^{PP}\cdot\mathbf{x}'} + A_\alpha^{SP}\,\mathrm{e}^{\mathrm{i}k_s\mathbf{k}^{SP}\cdot\mathbf{x}'} \tag{D.1}$$

and in the fluid it is

$$u_\alpha^{in}(\mathbf{x}') = A_\alpha^{FP}\, \mathrm{e}^{\mathrm{i}k_0 \mathbf{k}^{FP}\cdot \mathbf{x}'}, \tag{D.2}$$

where

$$A_\alpha^{P} = A_p k_\alpha^{p}, \qquad A_\alpha^{PP} = A_p k_\alpha^{PP} R_{PP}, \qquad A_\alpha^{SP} = A_p \varepsilon_{\alpha\gamma 2} k_\gamma^{SP} R_{SP}, \qquad A_\alpha^{FP} = A_p k_\alpha^{FP} T_{FP}, \tag{D.3}$$

with $k = k_p \sin\theta_i$. Similarly, for an incident S wave with amplitude A_s, the incident field in the solid is

$$u_\alpha^{in}(\mathbf{x}') = A_\alpha^{S}\, \mathrm{e}^{\mathrm{i}k_s \mathbf{k}^{S}\cdot \mathbf{x}'} + A_\alpha^{SS}\, \mathrm{e}^{\mathrm{i}k_s \mathbf{k}^{SS}\cdot \mathbf{x}'} + A_\alpha^{PS}\, \mathrm{e}^{\mathrm{i}k_p \mathbf{k}^{PS}\cdot \mathbf{x}'} \tag{D.4}$$

and in the fluid it is

$$u_\alpha^{in}(\mathbf{x}') = A_\alpha^{FS}\, \mathrm{e}^{\mathrm{i}k_0 \mathbf{k}^{F}\cdot \mathbf{x}'}, \tag{D.5}$$

where

$$A_\alpha^{S} = A_s \varepsilon_{\alpha\gamma 2} k_\gamma^{s}, \qquad A_\alpha^{SS} = A_s \varepsilon_{\alpha\gamma 2} k_\gamma^{SS} R_{SS}, \qquad A_\alpha^{PS} = A_s k_\alpha^{PS} R_{PS}, \qquad A_\alpha^{FS} = A_s k_\alpha^{FS} T_{FS}. \tag{D.6}$$

The forcing function in equation (3.9) is explicitly given by

$$b_{\alpha;m} = -\mathrm{i}mA_s\left(\frac{C_\alpha^{s+}}{k_s k_s^{+}}\, \mathrm{J}_m(ak_s^{+})\, \mathrm{e}^{-\mathrm{i}\gamma_s d} + \frac{R_{SS} C_\alpha^{s-}}{k_s k_s^{-}}\, \mathrm{J}_m(k_s^{-}a)\, \mathrm{e}^{\mathrm{i}\gamma_s d} + \frac{R_{PS} C_\alpha^{p-}}{k_p k_p^{-}}\, \mathrm{J}_m(ak_p^{-})\, \mathrm{e}^{\mathrm{i}\gamma_p d}\right), \tag{D.7}$$

with $k = k_s \sin\theta_i$. For an incident P wave, the expression is the same, but with the roles of P and S interchanged. For an incident F wave with amplitude A_f the incident field in the solid is

$$u_\alpha^{in}(\mathbf{x}') = A_\alpha^{PF}\, \mathrm{e}^{\mathrm{i}k_p \mathbf{k}^{PF}\cdot \mathbf{x}'} + A_\alpha^{SF}\, \mathrm{e}^{\mathrm{i}k_s \mathbf{k}^{SF}\cdot \mathbf{x}'} \tag{D.8}$$

and in the fluid it is

$$u_\alpha^{in}(\mathbf{x}') = A_\alpha^{F}\, \mathrm{e}^{\mathrm{i}k_0 \mathbf{k}^{F}\cdot \mathbf{x}'} + A_\alpha^{FF}\, \mathrm{e}^{\mathrm{i}k_0 \mathbf{k}^{FF}\cdot \mathbf{x}'}, \tag{D.9}$$

where

$$A_\alpha^{F} = A_f k_\alpha^{F}, \qquad A_\alpha^{FF} = A_f k_\alpha^{FF} R_{FF}, \qquad A_\alpha^{SF} = A_f \varepsilon_{\alpha\gamma 2} k_\gamma^{SF} T_{SF}, \qquad A_\alpha^{PF} = A_f k_\alpha^{PF} T_{PF}. \tag{D.10}$$

The forcing function is

$$b_{\alpha;m} = -\mathrm{i}mA_f\left(\frac{T_{SF} C_\alpha^{s-}}{k_s k_s^{-}}\, \mathrm{J}_m(k_s^{-}a)\, \mathrm{e}^{\mathrm{i}\gamma_s d} + \frac{T_{PF} C_\alpha^{p-}}{k_p k_p^{-}}\, \mathrm{J}_m(ak_p^{-})\, \mathrm{e}^{\mathrm{i}\gamma_p d}\right), \tag{D.11}$$

with $k = k_0 \sin\theta_i'$. Note that for $\theta_i' = \pm\theta_{cr}^{r}$, then $k = \pm k_r$ and the transmission coefficients are $O(1)$ rather than $O(\varepsilon)$. If $\theta_{cr}^{s} > |\theta_i'| > \theta_{cr}^{d}$, then the transmitted P wave is an inhomogeneous wave—that is, it propagates along the interface with exponential decay with depth—and if $|\theta_i'| > \theta_{cr}^{s}$, then both the transmitted P and S waves are inhomogeneous.

For an incident Schölte wave with amplitude A_{sch}, the incident wave in the solid is

$$u_\alpha^{in}(\mathbf{x}') = A_\alpha^{PSch}\, \mathrm{e}^{\mathrm{i}k_p \mathbf{k}^{PSch}\cdot \mathbf{x}'} + A_\alpha^{SSch}\, \mathrm{e}^{\mathrm{i}k_s \mathbf{k}^{SSch}\cdot \mathbf{x}'} \tag{D.12}$$

and in the fluid it is

$$u_\alpha^{in}(\mathbf{x}') = A_\alpha^{FSch}\, \mathrm{e}^{\mathrm{i}k_0 \mathbf{k}^{FSch}\cdot \mathbf{x}'}, \tag{D.13}$$

where $A_\alpha^{PSch} = A_{sch} k_\alpha^{PP}$, $A_\alpha^{SSch} = A_{sch} V \varepsilon_{\alpha\gamma 2} k_\gamma^{SS}$ and $A_\alpha^{FSch} = A_{sch} V_f k_\alpha^{FF}$, with $k = +k_{sch}$. The forcing function is

$$b_{\alpha;m} = -\mathrm{i}mA_{sch}\left(\frac{C_\alpha^{p-}}{k_p k_p^-}\,\mathrm{J}_m(ak_p^-)\,\mathrm{e}^{\mathrm{i}\gamma_p d} + \frac{VC_\alpha^{s-}}{k_s k_s^-}\,\mathrm{J}_m(ak_s^-)\,\mathrm{e}^{\mathrm{i}\gamma_s d}\right), \tag{D.14}$$

with $k = k_{sch}$. In the absence of the fluid, the case of an incident Rayleigh wave is identical, but with $k = +k_r$, and no wave in the fluid. The Schölte wave speed is

$$k_{sch} = k_s^2\left(\frac{1+\varepsilon}{2(k_s^2 - k_d^2)}\right)^{1/2} \exp\left(\frac{1}{2\pi}\int_{k_d}^{k_s} \tan^{-1}\phi_1 \frac{2\,\mathrm{d}\tau}{\tau} + \frac{1}{2\pi}\int_{k_s}^{k_0} \tan^{-1}\phi_2 \frac{2\,\mathrm{d}\tau}{\tau}\right). \tag{D.15}$$

The functions ϕ_1 and ϕ_2 are

$$\phi_1 = \frac{4\tau^2(\tau^2 - k_d^2)^{1/2}(k_s^2 - \tau^2)^{1/2} + \varepsilon k_s^4 k_0 (\tau^2 - k_d^2)^{1/2}/k_d (k_0^2 - \tau^2)^{1/2}}{(2\tau^2 - k_s^2)^2}, \tag{D.16}$$

$$\phi_2 = \frac{\varepsilon k_s^4 k_0 (\tau^2 - k_d^2)^{1/2}}{k_d (k_0^2 - \tau^2)^{1/2}((2\tau^2 - k_s^2)^2 - 4\tau^2(\tau^2 - k_d^2)^{1/2}(\tau^2 - k_s^2)^{1/2})}, \tag{D.17}$$

and the branch of the inverse tangent is chosen such that $0 \leqslant \tan^{-1}\phi \leqslant \pi$.

The scattered fields are of the form given in equations (5.2) and (5.3), and the functions $G_{P,S,F}(\theta, \phi)$ are

$$G_P(\theta, \phi) = 4\pi \frac{k_p^2}{k_s^2} \sum_{n=1}^{\infty} (-1)^n n\left(\frac{C_\alpha^{p+} a_{\alpha;n}}{k_p k_p^+}\,\mathrm{J}_n(ak_p^+)\,\mathrm{e}^{-\mathrm{i}\gamma_p d} + \frac{R_{PP} C_\alpha^{p-} a_{\alpha;n}}{k_p k_p^-}\,\mathrm{J}_n(ak_p^-)\,\mathrm{e}^{\mathrm{i}\gamma_p d}\right.$$

$$\left. + \frac{R_{SP} C_\alpha^{s-} a_{\alpha;n}}{k_s k_s^-}\,\mathrm{J}_n(ak_s^-)\,\mathrm{e}^{\mathrm{i}\gamma_s d}\right), \tag{D.18}$$

with $k = k_p \sin\phi$ and $-\pi/2 \leqslant \phi \leqslant \pi/2$. The corresponding shear directivity $G_S(\theta, \phi)$ is k_s^2/k_p^2 multiplied by the same expression, with the roles of P and S interchanged within equation (D.18), and with $k = k_s \sin\phi$. In the fluid the directivity function $G_F(\theta, \phi')$ is

$$G_F(\theta, \phi') = 4\pi \frac{k_0^2}{k_s^2} \sum_{n=1}^{\infty} (-1)^n n\left(\frac{T_{PF} C_\alpha^{p-} a_{\alpha;n}}{k_p k_p^-}\,\mathrm{J}_n(ak_p^-)\,\mathrm{e}^{\mathrm{i}\gamma_p d} + \frac{T_{SF} C_\alpha^{s-} a_{\alpha;n}}{k_s k_s^-}\,\mathrm{J}_n(ak_s^-)\,\mathrm{e}^{\mathrm{i}\gamma_s d}\right), \tag{D.19}$$

with $k = k_0 \sin\theta_i$ and $-\pi/2 \leqslant \phi' \leqslant \pi/2$. The angles ϕ and ϕ' are defined in the same sense as θ_i and θ_i' in Figure 3. The Schölte wave amplitudes are

$$H_P^{\pm}(\theta) = 2\pi \frac{k_p^2}{k_s^2 \gamma_p S'(k_{sch})} \sum_{n=1}^{\infty} n\left(\frac{S(k) R_{PP} C_\alpha^{p+} a_{\alpha;n}}{k_p k_p^+}\,\mathrm{J}_n(ak_p^+)\,\mathrm{e}^{\mathrm{i}\gamma_p d}\right.$$

$$\left. - \frac{S(k) R_{SP} C_\alpha^{s+} a_{\alpha;n}}{k_s k_s^+}\,\mathrm{J}_n(ak_s^+)\,\mathrm{e}^{\mathrm{i}\gamma_s d}\right), \tag{D.20}$$

with $k = \pm k_{sch}$.